Naval Research Laboratory

Stennis Space Center, MS 39529

Arabian Sea Mixed Layer Response to 1994-95 Operational Wind Products

Peter A. Rochford
John C. Kindle
Patrick C. Gallacher

Ocean Sciences Branch
Oceanography Division

Robert A. Weller

Physical Oceanography Department
Woods Hole Oceanographic Institution
Woods Hole, Massachusetts

September 29, 2000

REPORT DOCUMENTATION PAGE

Form Approved
OMB No. 0704-0188

1. AGENCY USE ONLY (*Leave Blank*)	2. REPORT DATE September 29, 2000	3. REPORT TYPE AND DATES COVERED Final

4. TITLE AND SUBTITLE

Arabian Sea Mixed Layer Response to 1994-95 Operational Wind Products

5. FUNDING NUMBERS

PE — 61153N
N00014-94-1-0161

6. AUTHOR(S)

Peter A. Rochford, John C. Kindle, Patrick C. Gallacher, and Robert A. Weller*

7. PERFORMING ORGANIZATION NAME(S) AND ADDRESS(ES)

Naval Research Laboratory
Oceanography Division
Stennis Space Center, MS 39529-5004

8. PERFORMING ORGANIZATION REPORT NUMBER

NRL/FR/7330--00-9948

9. SPONSORING/MONITORING AGENCY NAME(S) AND ADDRESS(ES)

Office of Naval Research
800 North Quincy Street
Arlington, VA 22217-5660

10. SPONSORING/MONITORING AGENCY REPORT NUMBER

11. SUPPLEMENTARY NOTES

*Woods Hole Oceanographic Institution, Woods Hole, MA

12a. DISTRIBUTION/AVAILABILITY STATEMENT

Approved for public release; distribution is unlimited.

12b. DISTRIBUTION CODE

13. ABSTRACT (*Maximum 200 words*)

The evolution of the upper ocean in the strong seasonally forced Arabian sea, as observed by a mooring deployed from 1994 to 1995, is investigated using the Naval Research Laboratory Layered Ocean Model (NLOM). Model simulations were sensitive to the choice of surface wind products used for forcing, and results are reported for simulations forced by monthly mean climatologies and 12-hourly 1994-95 wind products from two operational atmospheric forecast models, the European Centre for Medium-Range Weather Forecast (ECMWF) model and the Navy Operational Global Atmospheric Prediction System (NOGAPS) model of the Fleet Numerical Meteorology and Oceanography Center (FNMOC). The NLOM yields the best prediction of sea surface temperature (SST) and mixed layer depth (MLD) when using FNMOC forcing. Surface cooling is found to be responsible for the seasonal SST minimum during the northeast (NE) monsoon. Heat advection is found to be important for supporting the surface cooling during the second half of the NE monsoon. Strong entrainment and appreciable advective cooling are responsible for the SST minimum of the southwest (SW) monsoon. The NLOM wind experiments strongly suggest that thermal convection may be important in the central Arabian Sea during the winter months.

14. SUBJECT TERMS		15. NUMBER OF PAGES 47
Upper ocean	OGCM	
Mixed layer		16. PRICE CODE
Wind forcing		

17. SECURITY CLASSIFICATION OF REPORT	18. SECURITY CLASSIFICATION OF THIS PAGE	19. SECURITY CLASSIFICATION OF ABSTRACT	20. LIMITATION OF ABSTRACT
UNCLASSIFIED	UNCLASSIFIED	UNCLASSIFIED	UL

CONTENTS

ARABIAN SEA MIXED LAYER RESPONSE TO 1994-1995 OPERATIONAL WIND PRODUCTS

1. INTRODUCTION

The Arabian Sea experiences strong surface forcing from the winds of the regularly alternating northeast (November to February) and southwest (June to September) monsoons. The northeast (NE) monsoon is characterized by winds of up to 10 $\mathrm{m\,s^{-1}}$ from the northeast, parallel to the coast of Somalia. The stronger southwest (SW) monsoon has wind speeds of up to 18 $\mathrm{m\,s^{-1}}$ in the opposite direction, with the strongest winds concentrated in July over the western Arabian Sea in a feature called the Findlater Jet. The winds influence sea surface temperature (SST) by driving turbulent mixing, which entrains deeper, colder water; by forcing coastal and open ocean upwelling; and by forcing horizontal advection, which brings cool water upwelled along the Arabian and Somali coasts into the central Arabian Sea and warm water north from the equator.

Surface heat fluxes also play a central role in forcing the Arabian Sea. The consequences of this forcing are not simple to interpret, as a feedback is possible between the SST change and the surface heat fluxes. The lower SST that results from mixed layer deepening can result in greater surface heating because of the SST dependence of the longwave, latent, and sensible components of the net surface heat flux. This would oppose the tendency of the mixed layer to deepen.

Efforts to better understand the forced response of the upper ocean in the Arabian Sea have often in the past used ocean general circulation models (OGCMs) (Kindle 1991, McCreary and Kundu 1989, McCreary et al. 1993). However, the lack of in-situ data has made it difficult to assess the realism achieved by such models, especially when forced by surface wind and heat fluxes that themselves had large uncertainties. Still, because of the energetic large and mesoscale circulation in the Arabian Sea, a local field study may not collect the data needed to determine the impact of larger scales on the local evolution of the mixed layer. In this study, we use both new in-situ data and an OGCM to address these problems.

As part of a recent cooperative research effort, year-long time series have been obtained from a mooring in the central Arabian Sea (Weller et al. 1998). The mooring provides the records of local forcing and local response. An OGCM (the Naval Research Laboratory Layered Ocean Model (NLOM)) is used to supplement the mooring data and provide information about the larger scale variability in which the mooring was located. However, because the model circulation depends on which of several available wind fields is applied as forcing, we also examine the sensitivity of the OGCM predictions of mixed layer depth (MLD) and SST to the choice of forcing fields.

In doing this study, we had three goals: to examine the relationship between wind forcing and mixed layer dynamics in the Arabian Sea, to contribute to the interpretation of the upper ocean

variability observed at the mooring by using the NLOM, and to assess the predictive capability of the NLOM. The OGCM is fully described in Section 2. A variety of forcing fields (described in Section 3) are used to force a suite of model simulations to explore the causal relationship between the forcing and the upper ocean dynamics. OGCM experiments using different wind products are described in Section 4. Sections 5 through 7 discuss the OGCM simulations of the SST, MLD, and currents at the location of the moored array. The surface heat fluxes from the model runs are compared to those observed at the moored array as a check on the realism of the model in Section 8. Section 9 discusses the heat balances for the mixed layer and uppermost dynamical layer. Finally, Section 10 presents our summary and conclusions.

Four appendix are included in this report to provide more detailed information on specific aspects of the NLOM. Appendix A describes the oxygen-based diapycnal mixing scheme used in the NLOM for the global mixing correction scale factors. Appendix B provides a useful list of the many symbols used in the equations throughout the report. Appendix C presents the detailed derivation of the heat equation used for the heat balance results reported here. Finally, Appendix D provides a glossary of acronyms used in this report.

2. THE MODEL OCEAN

The model used for this study is the reduced-gravity version of the NLOM with modifications to embed a surface mixed layer. The model without the mixed layer has already been well-described in Hurlburt et al. (1996) and Metzger and Hurlburt (1996), and been used to examine the Arabian Sea circulation by Bruce et al. (1994), Keen et al. (1997), and Young and Kindle (1994). The reader is referred to these for the details on the circulation component. In the modified model used here, the surface mixed layer is embedded within the upper layer of the circulation model in a manner similar to the "fossil layer" approach first developed by McCreary and Kundu (1989), and later augmented by them for the Indian Ocean basin (McCreary et al. 1993, MKM hereafter). The reader is referred to these references for the physical rationale and layer dynamics of this approach.

2.1 Layer Model

The NLOM has prognostic equations of motion for transport ($\mathbf{V}_k$), density (ρ_k), and layer thickness (h_k) as given in Metzger and Hurlburt (1996). We follow their notation throughout this manuscript[1]. Four significant changes were made to the OGCM to accommodate the presence of the mixed layer and improve upon the OGCM simulation.

The first change is the vertical mixing velocity for the first interface (ω_1) now includes a contribution due to turbulent entrainment (ω_{kt}) whenever the mixed layer has merged with the first layer.

$$\omega_k = \begin{cases} 0, & k = 0 \\ \omega_k^+ + \delta_{1k}\omega_m^+ - \omega_k^- - \Omega_k\widehat{\omega}_k, & k \geq 1 \end{cases} \tag{1}$$

$$\omega_m^+ = \begin{cases} 0 & \text{for } h_1 > h_m \\ \max(0, \omega_{kt}) & \text{for } h_1 \leq h_m \end{cases} \tag{2}$$

The definition of ω_{kt} is given further below (*cf* Section 2.2).

---

[1]Physical quantities which are obtained from a climatology will be denoted by a caret (⌢) throughout this report.

The second change is the use of a monthly varying climatology $(\widehat{\rho_k})$ in the relaxation term of the density equation $\sigma_\rho(\widehat{\rho_k} - \rho_k)$ (*cf* Eq. (A2) in Metzger and Hurlburt (1996)). Traditionally, the NLOM has relaxed the layer densities to an annual mean density based on Levitus (1982). However, from NLOM trial simulations with the embedded mixed layer, it was found necessary to relax the layer densities to a monthly varying climatology in order to get the correct seasonal variation in the layer 1 temperature. By this we mean the σ_ρ varies each month, with the monthly mean $\widehat{\rho_k}$ interpolated in time between the midpoints of the months. Here, the relaxation time scale (σ_ρ^{-1}) is equal to the length of the month. The monthly mean $\widehat{\rho_k}$ is determined using monthly mean layer thicknesses (h_k) obtained from multiyear NLOM simulations during the spin up phase (*cf* Section 2.3). The layer densities are obtained from the monthly temperature and salinity climatologies of Levitus et al. (1994, 1994a) using an equation of state with zero pressure (Millero and Poisson 1981) to be consistent with the NLOM assumption of an incompressible ocean. The annual Levitus climatology is used to supplement the monthly climatology at depths beyond 1000 m.

The third change, the thermal expansion coefficient (α), has been given a temperature dependence to accomodate global scale modeling.

$$\alpha(T) = -\frac{1}{\rho_0}\frac{\partial\rho}{\partial T}$$
$$= \frac{1}{\rho_0}(a_1 + 2a_2 T). \tag{3}$$

This is derived from the assumed equation of state

$$\rho(T, S) = a_0 - a_1\,T - a_2\,T^2 + a_S(S - S_0), \tag{4}$$

which is fitted using the global annual Levitus climatologies for temperature T and salinity S. Table 1 gives the parameter values. The values $(a_0, a_1, a_2, a_S, S_0)$ are obtained by using the same equation of state as above and then applying a least squares fit to all densities with salinities between 30 and 40 psu and temperatures between 10° and $25\,^\circ$C. Earlier NLOM studies (Metzger and Hurlburt 1996) assumed a linear dependence of layer density on layer temperature to obtain the heat flux forcing term in the density equation. A temperature-dependent thermal expansion is included here to accommodate global scale modeling, where significant density deviations would occur due to the zonal temperature variations. The climatological temperature for the layer $(\widehat{T_k})$ is chosen as the most appropriate value to use for the temperature dependence.

Table 1 — Parameters for Fitted Equation of State

Parameter	Value
ρ_0	1023.0 kg m^{-3}
a_0	28.27 σ_t
a_1	0.0872 $\sigma_t\,^\circ C^{-1}$
a_2	0.0044 $\sigma_t\,^\circ C^{-2}$
a_S	0.7674 σ_t
S_0	35.0 psu

In the NLOM interlayer mixing scheme (Hurlburt et al. 1996), the weighting factor Ω_k is parameterized to represent the climatological cross-isopycnal detrainment rate, by basing it on annual oxygen saturation values at the mean interface depths (Levitus and Boyer 1994b). Here we calculate Ω_k using a variation of the original diapycnal mixing scheme (Shriver and Hurlburt 1997) to remove anomalous results that occured with the original formulation. The details are given in Appendix A.

2.2 Mixed Layer Model

The surface turbulent boundary layer that is embedded within the OGCM is assumed to be "well mixed." The temperature T_m is therefore defined to be constant throughout a layer of thickness h_m, where the latter has a minimum thickness of a few meters. The layer thickness h_m is defined as the lower bound of the turbulent boundary layer and is hence the MLD. The SST and MLD prognostic equations are consistent with the NLOM dynamical equations for layer 1, and their notation is given in Appendix B.

SST:

$$\frac{\partial T_m}{\partial t} + \mathbf{v}_1 \cdot \nabla T_m = -\frac{\max(0, \omega_m)}{h_m}(T_m - T_e) + \frac{Q}{\rho_o C_p h_m} + \frac{K_H}{h_m} \nabla \cdot (h_m \nabla T_m) \tag{5}$$

MLD:

$$\frac{\partial h_m}{\partial t} + \nabla \cdot (h_m \mathbf{v}_1) = \omega_m \,. \tag{6}$$

Note that the horizontal velocity within the mixed layer is assumed to be the same as the first dynamical layer. The vertical mixing velocity is given by

$$\omega_m = \begin{cases} \omega_{kt} & \text{for } h_m < h_1 \\ \omega_{kt} + \omega_1 & \text{for } h_m \geq h_1 \,, \end{cases} \tag{7}$$

where ω_{kt} is the rate of mixed layer deepening or retreat as discussed below. Although $h_m > h_1$ is allowed in the calculation of ω_m and ω_1, $h_m \leq h_1$ is enforced for numerical stability at the end of each time step.

The temperature T_e is that of water entrained into the mixed layer from the thermocline below. Its value must be obtained by parameterizing the thermocline in terms of model variables (T_1, T_m, T_2, h_1, h_m, and h_2). After testing several parameterizations (Gallacher 1994, Gallacher and Peggion 1999), we found that a simple linear model yielded the best combination of accuracy and robustness for providing an entrainment temperature.

$$T_e = T_1 + \frac{h_m}{h_1 + \frac{1}{2}h_2} \left(T_2 - T_1\right) \tag{8}$$

The temperature T_k of the kth dynamic layer is calculated from the density of the layer.

$$T_k = \widehat{T_k} - \frac{\rho_k - \widehat{\rho_k}}{\alpha(\widehat{T_k})\rho_o} \tag{9}$$

Here $\widehat{\rho_k}$ is the k$^{\text{th}}$ layer density climatology, and $\widehat{T_k}$ the corresponding temperature climatology. The departures of layer density (ρ_k) from the monthly mean climatology ($\widehat{\rho_k}$ and $\widehat{T_k}$) are assumed to be solely due to temperature, as there is no explicit treatment of salinity in the NLOM, and there is no surface forcing applied due to evaporation minus precipitation ($E - P$). The contribution from salinity can be incorporated into the model in the future when the fluxes of fresh water are better known.

The rate of mixed layer deepening or retreat ω_{kt} is determined using a modified version of the Kraus-Turner mixed layer model (Kraus and Turner 1967, Niiler and Kraus 1977, Gallacher and Peggion 1999). The turbulent kinetic energy (TKE) budget is assumed to be one dimensional (the vertical fluxes are much larger than the horizontal fluxes) and stationary ($de/dt = 0$). The terms in the TKE budget are parameterized using variables integrated through the mixed layer and surface fluxes:

$$\begin{aligned}
\int \frac{de}{dt} dz &= m_3 u_*^3 - \frac{n}{2} b_* w_* h_m - \frac{h_m}{2} \overline{b'w'}(-h_m) \\
&\quad -(m_1 u_*^3 - \delta m_6 b_* w_* h_m + m_5 \widetilde{f} u_*^2 h_m) \\
&= 0.
\end{aligned} \tag{10}$$

The first term on the right hand side is the shear production of TKE generated by the surface wind stress (τ), $u_*^2 = |\tau|/\rho_o$ is the friction velocity, and e is the TKE. The second term is the production or damping of TKE by surface buoyant forcing:

$$b_* w_* = \frac{g\alpha(T_m)Q}{\rho_o C_p}. \tag{11}$$

The third term is the increase in potential energy in the mixed layer due to entrainment:

$$-\overline{b'w'(-h_m)} = \alpha(T_m)g\Delta T_m \frac{\partial h_m}{\partial t}. \tag{12}$$

To be consistent with the equation for T_m, we should have $\Delta T_m = T_m - T_e$. However, it was found in practice that the mixed layer became too deep during the intense boreal summer cooling in the southern Indian Ocean. In order to obtain mixed layer depths consistent with climatology (Rao et al. 1989) we had to use values of $\Delta T_m = 4°C$. This is consistent with the results of McCreary et al. (1993).

The last terms represent the turbulent dissipation of TKE. The first term in the dissipation parameterization is a fixed fraction of the shear production. The second term is a fraction of the buoyant production of TKE, thus

$$\delta = \begin{cases} 1, & \text{for } b_* w_* < 0 \\ 0, & \text{for } b_* w_* \geq 0. \end{cases} \tag{13}$$

The third term was not included in the original Kraus-Turner model. It incorporates the Coriolis time scale into the dissipation parameterization,

$$\widetilde{f} = \max(|f|, f_*), \tag{14}$$

where $f_* = 2.54 \times 10^{-5} \, s^{-1}$ is the Coriolis parameter at 5° latitude. This is particularly important for deep mixed layers (Garwood 1977) and to provide the correct asymptotic depth in the neutral limit (Blackadar and Tennekes 1968).

The model constants were determined from one-dimensional simulations of several idealized cases of wind-stirring, heating, and cooling. The mixed layer model was further tested with one-dimensional simulations of the seasonal cycle of mixed layer deepening and retreat at Ocean Weather Station Papa (Gallacher and Peggion 1999). The model was also tested in an idealized two-dimensional study of air-sea interaction during coastal upwelling (Gallacher and Peggion 1999). The values of the model constants are given in Table 2 (see Appendix B for notation).

Table 2 — Turbulence Model Parameters

Parameter	Value
C_p	$3988 \, \mathrm{J \, kg^{-1} \, {}^\circ C^{-1}}$
Δt	24 min
ΔT_m	$4 \, {}^\circ\mathrm{C}$
f_*	$2.54 \times 10^{-5} \, s^{-1}$
g	$9.8 \, \mathrm{m \, s^{-2}}$
h_m^+	20 m
m_1	$5.0 \, m^{-1}$
m_3	$7.5 \, m^{-1}$
m_5	5.0
m_6	0.15
n	1

When the production of TKE exceeds the dissipation and damping of TKE, the mixed layer deepens until the increase in potential energy from entraining colder water equals the available TKE (ATKE). The rate of mixed layer deepening

$$\begin{aligned} \omega_{kt} &= \frac{\partial h_m}{\partial t} \\ &= \frac{h_{eq} - h_m^-}{2\Delta t}, \end{aligned} \tag{15}$$

is computed by calculating the equilibrium depth h_{eq} at which this balance is achieved from Eq. (10) at the latest time step, and evaluating its change relative to the mixed layer depth at the previous leapfrog time step h_m^-. The equilibrium depth is given by

$$h_{eq} = h_m^- + \mathrm{ATKE}/(\alpha g \Delta T_m h_m^-), \tag{16}$$

where energy is assumed to be converted solely by entrainment of water that is ΔT_m colder than the mixed layer. When the production of TKE is less than the dissipation and damping of TKE, the mixed layer retreats to an equilibrium depth given by

$$h_{eq} = \frac{m_3 u_*^3 - m_1 u_*^3}{\frac{n}{2} b_* w_* - \delta m_6 b_* w_* + m_5 \widetilde{f} u_*^2}. \tag{17}$$

The mixed layer TKE budget is assumed to be stationary, i.e., production, dissipation, and mixing are in balance. To be consistent with this assumption, the mixed layer is defined to instantaneously adjust to the equilibrium depth h_{eq} rather than as a relaxation to this depth with a characteristic time scale. Finally, a minimum MLD of $h_m^+ = 20\,\mathrm{m}$ is imposed in order to maintain numerical stability.

2.3 Model Basin, Boundary Conditions, and Initial Conditions

The model domain and boundary conditions are identical to those used in earlier Indian Ocean studies (Young and Kindle 1994, Bruce et al. 1994, Gallacher and Rochford 1995). A version of the NLOM is formulated for this study with three active layers within the upper $550\,\mathrm{m}$. The fourth lowest layer (encompassing the volume below $\sim 550\,\mathrm{m}$) is infinitely deep and at rest, as required in a reduced gravity formulation. The initial undisturbed layer thicknesses are given in Table 3, along with the complete list of model parameters used in all the experiments reported here.

Table 3 — NLOM Parameters for Indian Ocean Simulations

| Parameter | Value | | | |
	Const.	k=1	k=2	k=3
A_H	$300\,\mathrm{m^2\,s^{-1}}$	$\cdots$	$\cdots$	$\cdots$
H_o	$100\,\mathrm{m}$	$\cdots$	$\cdots$	$\cdots$
K_H	$5000\,\mathrm{m^2\,s^{-1}}$	$\cdots$	$\cdots$	$\cdots$
H_k	$\cdots$	115	200	$235\,\mathrm{m}$
h_k^+	$\cdots$	60	75	$75\,\mathrm{m}$
h_k^-	$\cdots$	500	600	$1000\,\mathrm{m}$
$\tilde{\omega}_k$	$\cdots$	0.01	0.01	$0.01\,\mathrm{m\,s^{-1}}$
C_k	$\cdots$	0.0	0.0	0.0
$\Delta\rho_k^+$	$\cdots$	0.05	0.05	$0.05\,\mathrm{kg\,m^{-3}}$

The model layer density and global detrainment climatologies are initialized by vertically integrating the Levitus climatology for these initial layer thicknesses. The initial velocity field is then determined by running the model, with no mixed layer, from a state of rest to statistical equilibrium of the domain-averaged kinetic and potential energy for each layer. The model is forced with the monthly mean wind stress climatology of Hellerman and Rosenstein (HR) (1983) and no heat fluxes during this phase. The model was spun up for 10 years, and density $(\widehat{\rho}_k)$ and temperature $(\widehat{T}_k)$ climatologies were constructed from the monthly mean layer thicknesses of years 8 to 10, and the global detrainment climatology was constructed from the corresponding annual mean layer thicknesses. This 10 year spin up serves as the initial state for the subsequent spin up of the mixed layer experiments with the different wind products.

3. SURFACE FORCING

3.1 Surface Wind Stresses

We examine the sensitivity of the mixed-layer response to three wind stress products from two operational weather forecast models as well as wind stresses from a well-known monthly climatology.

By comparing the responses to these different wind products, the sensitivity of the mixed layer to short-term wind events in the operational wind stresses can be determined.

For the climatological experiments we use the monthly surface wind stress climatology of Hellerman and Rosenstein (1983), and the wind velocities from the Comprehensive Ocean-Atmosphere Data Set (COADS) (da Silva et al. 1994). The COADS wind velocities are used in the heat flux forcing (*cf* Section 3.2) and are at a nominal reference height of 20 m above sea level. For the first operational wind experiment we use a 1990-96 data set of 12-hourly wind velocities at 1000 mb pressure elevation from the European Centre for Medium-Range Weather Forecast (ECMWF) model (ECMWF Research Department 1988, 1991, ECMWF Technical Attachment 1993). For the remaining experiments we use 1990-96 data sets of 12-hourly surface wind stresses and 10 m wind velocities from the Navy Operational Global Atmospheric Prediction System (NOGAPS) model at Fleet Numerical Meteorology and Oceanography Center (FNMOC) (Hogan and Rosmond 1991).

For the ECMWF product, we use the standard bulk formula to construct wind stresses (τ) from the 1000 mb winds ($\mathbf{v}$)

$$\tau = \rho_a C_d |\mathbf{v}| \mathbf{v}, \qquad (18)$$

where ρ_a is the density of air and C_d is a constant drag coefficient. To obtain a wind stress with a magnitude consistent with the HR wind stresses, we construct a pseudo stress $|\mathbf{v}|\mathbf{v}$ from the monthly mean climatology of these winds, and scale their Arabian Sea average to be similar to the HR wind stresses at the height of the southwest (SW) monsoon. No consideration is given to the height of the 1000 mb surface in calculating the wind stress. This scaling is validated by comparing a 1994-1995 time series of the ECMWF wind stresses against those computed from the Woods Hole Oceanographic Institution (WHOI) mooring meteorological observations (Weller et al. 1998). When this same method is applied to the FNMOC surface streses, we find the wind stress is underestimated at the peak strength of the SW monsoon. The FNMOC surface stresses are therefore multiplied by $\lambda_\tau = 1.35$ to bring them into better agreement.

The time series of the wind speeds from the various wind products compare well with the moored buoy data over most of the 1994-1995 sampling period (Fig. 1). (Throughout this manuscript, 12-hourly averages of the mooring record are used to be consistent with the highest frequency of the wind products.) A 5-day moving average is applied to help distinguish the differences between the wind products. Wind speed differences with respect to the buoy are on the order of 2-3 m s^{-1} outside the SW monsoon, and differ by up to 2-3 m s^{-1} during the SW monsoon. The ECMWF 1000 mb winds consistently overestimate the buoy wind speed and the COADS winds consistently underestimate outside the SW monsoon period. The former is likely because the 1000 mb pressure height is usually closer to the ocean surface than 10 m, and would have a greater strength according to a $\log(z/z_0)$ wind profile. The reason the COADS wind speed underestimates the buoy wind speed is likely because they are constructed from ship observations taken at a nominal reference height of 20 m (da Silva et al. 1994) and would therefore be weaker than the 10 m winds. The wind scale parameters (Table 4) yield wind stresses that also compare favorably with the buoy observations (Fig. 2). Note that adjustment of the $\rho_a C_d$ values allows these constructed wind stresses to be in better agreement with the buoy wind stresses than the operational winds with the buoy winds. The largest differences in wind stress with respect to the buoy again occur during the SW monsoon.
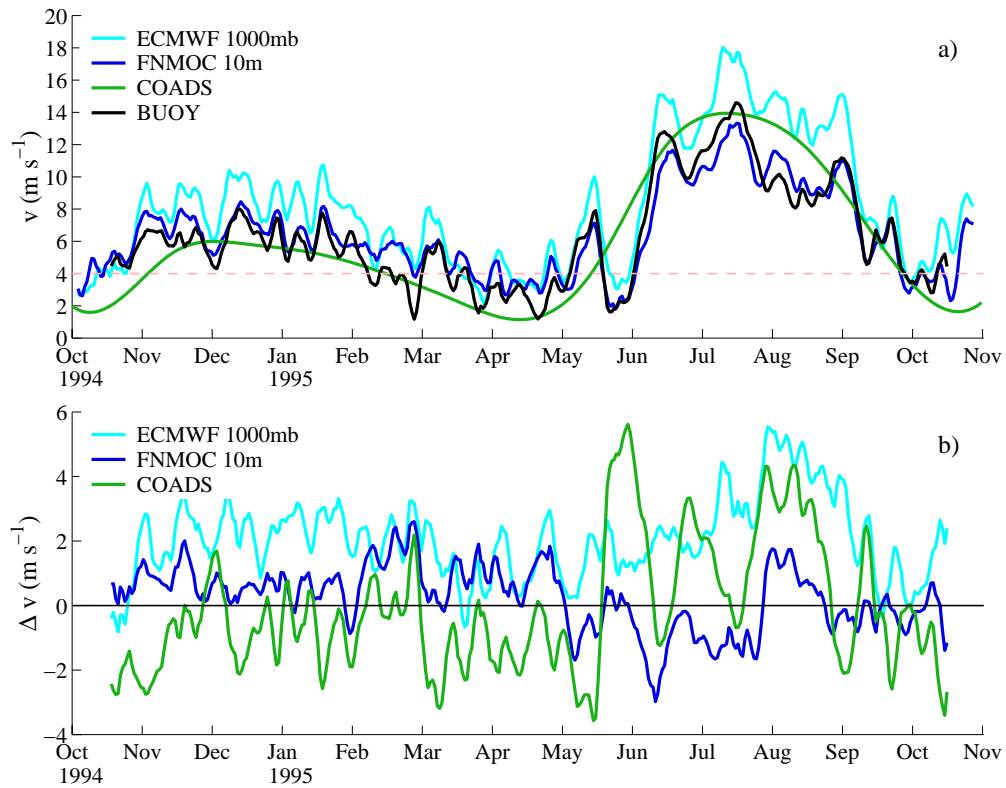
Fig. 1 — a) Time series of wind speeds at the WHOI mooring location (15.5°N, 61.5°E) from four wind products: the COADS climatology (COADS), the ECMWF 1000 mb winds (ECMWF), the FNMOC 10 m winds (FNMOC 10m), and the WHOI buoy Vector-Averaging Wind Recorder (VAWR) data (BUOY). A five-day moving average was applied to the operational and buoy winds to smooth out the data. The minimum wind speed used in the heat flux calculations is indicated for reference. b) Differences between the wind speeds of the wind products and the mooring.
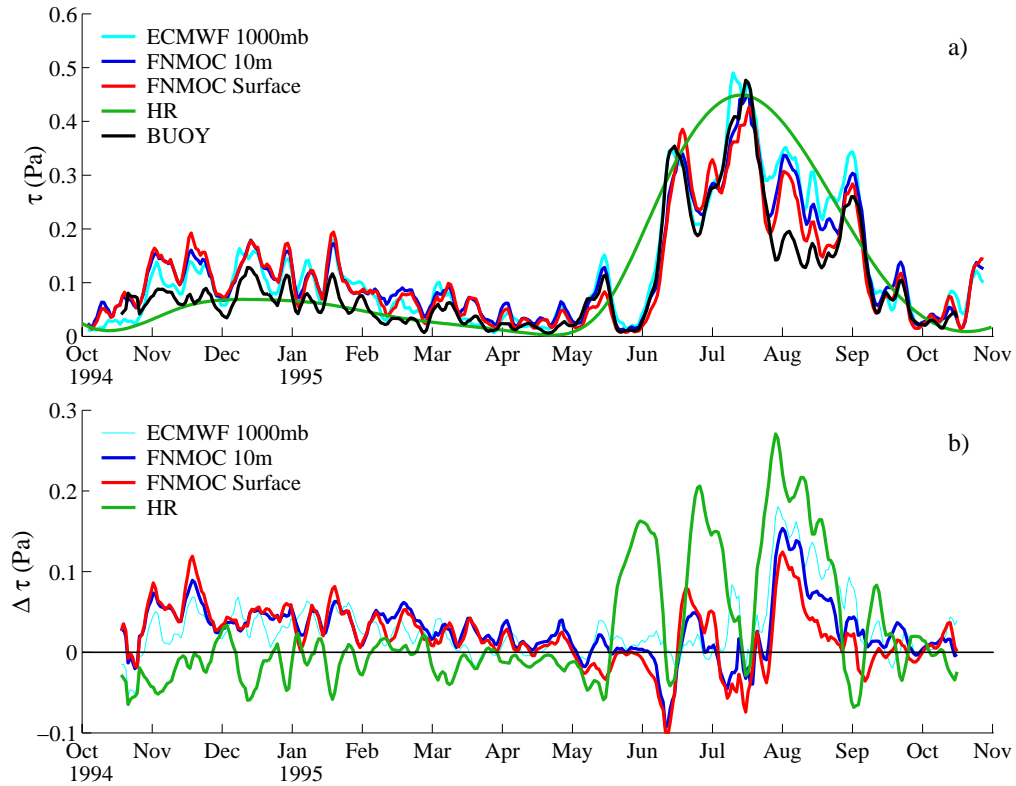
Fig. 2 — a) Time series of wind stresses at the WHOI mooring location (61.5°E, 15.5°N) from five wind products: the ECMWF 1000 mb winds (ECMWF), the FNMOC 10 m winds (FNMOC 10m), the FNMOC surface wind stresses (FNMOC Surface), the HR climatology (HR), and the wind stresses computed from the WHOI buoy meteorology data (BUOY). A five-day moving average was applied to smooth out the data. b) Differences between the wind stresses of the wind products and the mooring.

Table 4 — NLOM Experiments

Expt.	Wind Stress	Wind Velocity	Resolution	λ_τ	$\rho_a C_d$
Clim.	HR	COADS	2° & 1°	1.00	$\cdots$
ECMWF	ECMWF 1000 mb	ECMWF 1000 mb	2.5°	1.00	1.5×10^{-3}
FNMOC	FNMOC Surface	FNMOC 10 m	1.25°	1.35	$\cdots$
FNMOC 10m	FNMOC 10 m	FNMOC 10 m	1.25°	1.00	2.52×10^{-3}

The good agreement between the wind products and observations is evident from the high values of the correlation coefficients r for both the wind speeds and wind stresses. These correlation coefficients are determined using daily average values of the wind speeds and wind stresses (Table 5)[2]. To obtain a measure of the predictive skill of the different wind products, we have also included in Table 5 the nondimensional skill score (Murphy 1995):

$$SS(x, y) = 1 - \frac{rmse(x, y)^2}{\sigma(y)^2} \qquad (19)$$

where $rmse(x, y)$ is the root-mean-square-error between x and y, and $\sigma(y)^2$ is the variance of the reference value y (i.e., mooring observations). All wind products are interpolated to the same grid resolution for the simulations, which is at $2\Delta x$ of the model grid. A detailed comparison of the time series of these different wind products may be found in Weller et al. (1998).

Table 5 — Correlations and Skill Scores for Wind Products

	(Wind Prod, Buoy)			
Wind Prod	$r(\tau, \tau)$	$SS(\tau, \tau)$	$r(v,v)$	$SS(v,v)$
COADS	$\cdots$	$\cdots$	0.83	0.53
ECMWF	0.92	0.72	0.94	0.38
FNMOC 10m	0.92	0.77	0.93	0.85
FNMOC Surface	0.91	0.78	$\cdots$	$\cdots$
HR	0.83	0.36	$\cdots$	$\cdots$

3.2 Surface Heat Fluxes

The COADS monthly mean atmospheric climatology is used to calculate the surface heat flux forcing (da Silva et al. 1994). The forcing is calculated following the same approach as McCreary and Kundu (1989). The heat flux at the ocean's surface is considered to be a sum of four parts: incoming solar shortwave radiation, outgoing longwave radiation, sensible heat flux (Q_S), and latent heat flux (Q_L). We elect to follow the MKM and do not include model SST dependence in the outgoing longwave radiation. Instead we construct a net radiation ($\widehat{Q}_R$) forcing from the addition of the shortwave and longwave radiation climatologies. Only the sensible and latent heat fluxes have a dependence on the model SST in the NLOM net heat flux:

---

[2]All correlation coefficients reported in this manuscript are found to be statistically significant upon applying the "no correlation" test described by Chu et al. (1998).

$$Q = \widehat{Q}_R + Q_S + Q_L. \tag{20}$$

The sensible heat flux depends only on the air-sea temperature difference and the surface wind speed. The latent heat flux depends on these as well as the air-sea difference in specific humidity. The latter requires calculating the saturated specific humidity (q_s) at the sea surface temperature (T_m). The heat fluxes are given by the expressions

$$\begin{aligned} Q_S = C_S \, C_{pa} \, \rho_a \max(v_{min}, \widehat{v_a}) \\ \times \left(\widehat{T_a} - T_m \right) \end{aligned} \tag{21}$$

$$\begin{aligned} Q_L = C_L \, L \, \rho_a \max(v_{min}, \widehat{v_a}) \, (\widehat{q_a} - q_s) \\ \times \Theta(q_s - \widehat{q_a}) \leq 0 \end{aligned} \tag{22}$$

$$C_L = C_{L0} + b(T_m - \widehat{T_a}) \tag{23}$$

$$q_s = \frac{\epsilon e_s}{P_a - (1 - \epsilon)e_s} \tag{24}$$

$$e_s = 6.1078 \exp\left(\frac{19.33 T_m}{T_m + 273.15} \right), \tag{25}$$

where the symbols are defined in Appendix B and the parameter values are given in Table 6. We adopt the oceanographic sign convention of positive heat fluxes downwards. Note that the empirical coefficient C_L is assigned an increasing value with air-sea temperature difference to simulate its observed effect on atmospheric stability, and that it is limited to a range of reasonable values $0.001 \leq C_L \leq 0.002$. The COADS climatology is used for both the temperature and specific humidity of the atmosphere in these expressions.

The surface wind speed v_a is constrained to have a minimum value of v_{min}. This is to account for nonzero latent and sensible heat flux as the wind speed goes to zero. A value of $v_{min} = 4 \text{ m s}^{-1}$ was found to yield the optimal agreement. This was determined by computing the net surface, latent, and sensible heat fluxes at the WHOI mooring location using the COADS wind speed and SST, and then comparing the time series against the monthly COADS heat fluxes at the same location. This threshold value for v_{min} is consistent with an analysis of data from the western equatorial Pacific

Table 6 — Surface Heat Flux Parameters

Parameter	Value
C_S	0.001
C_{pa}	$1012 \text{ J kg}^{-1}\,^{\circ}\text{C}^{-1}$
C_{L0}	0.0015
b	$0.00033 \,^{\circ}\text{C}$
ϵ	0.62197
L	$2.44 \times 10^6 \text{ J kg}^{-1}$
P_a	1013 mb
ρ_a	1.1275 kg m^{-3}
v_{min}	4 m s^{-1}

Ocean, where derived bulk transfer coefficients were found to increase rapidly with a decreasing wind speed below $4 \mathrm{\,m\,s}^{-1}$ (Greenhut and Khaksa 1995).

4. WIND EXPERIMENTS

Four model simulations were performed to examine the mixed layer sensitivity to wind products (Table 4). The first simulation is forced by the HR and COADS wind products to see the Arabian Sea response to the seasonal reversals in monsoon winds (referred to henceforth as the HR-COADS Expt.). The second simulation used the ECMWF wind product (ECMWF Expt. henceforth). The 12-hourly interannual variability of this wind product is the major difference with respect to the climatological wind forcing. The third experiment uses the surface stresses (henceforth FNMOC Expt.). The fourth experiment (henceforth FNMOC 10m Expt.) uses wind stresses constructed from the 10 m winds in the same manner as the ECMWF wind stresses (Section 3.1), with an appropriate value for the drag coefficient (Table 4). The latter two FNMOC experiments are performed to explore the sensitivity of the mixed layer to the effects of atmospheric stability on surface stress, as the FNMOC surface stresses include the effects of dynamic stability within the atmospheric planetary boundary layer. The 10 m wind velocities are used in the heat flux forcing for both FNMOC experiments.

The models are spun up from the initial state (*cf* Section 2.3) with heat fluxes obtained with an active mixed layer. For the operational wind experiments, the model is first forced using a monthly mean wind climatology constructed from years 1990-96 of their wind stresses and no heat fluxes to bring the model to equilibrium. They are then run using using the 12-hourly winds from January 1990 to January 1996, starting with the 0Z hour wind of January 15, 1990. This choice of calendar day coincides with the end of the climatological wind cycle, which terminates at the monthly mean for January.

5. SEA SURFACE TEMPERATURE

The NLOM reproduces quite well the seasonal variability in the SST as given by the mooring record and the climatology (COADS) when forced by the climatological and operational wind products (Figs. 3a-b). The largest differences between the model and buoy SST are at most $1.5\,^{\circ}\mathrm{C}$. The SST decrease during the NE and SW monsoons (Table 7) closely follows the deepening of the mixed layer (Fig. 6), indicating the importance of entrainment for bringing deeper colder water into the mixed layer, and thereby cooling the surface waters. It is noteworthy that the NLOM hindcasts a comparable peak SST value to that found in mid-May of 1995 in the mooring record.

Table 7 — Arabian Sea Monsoons

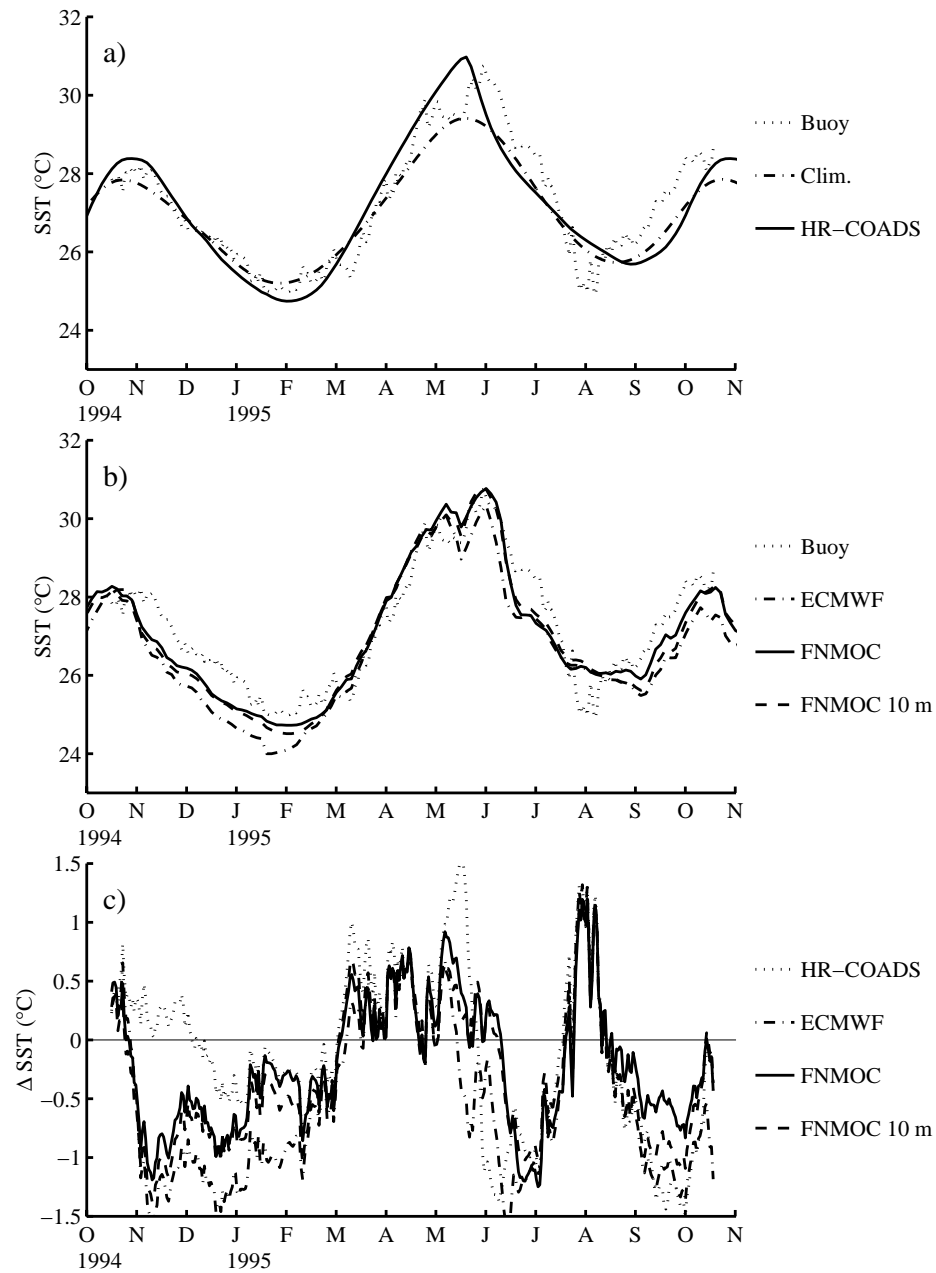| Monsoon	Start	End
1994 NE Monsoon	Nov. 1	Feb. 15
1995 Spring Intermonsoon	Feb. 16	May 31
1995 SW Monsoon	Jun. 1	Sep. 15
1995 Fall Intermonsoon	Sep. 16	Oct. 15

Fig. 3 — Time series of SST from the four wind experiments: a) climatological winds (HR-COADS), b) ECMWF 1000 mb winds, FNMOC surface stresses and 10 m winds (FNMOC), and FNMOC 10 m winds (FNMOC 10m). The SST from the WHOI mooring (Buoy) and from the COADS climatology (COADS) are included in a) and b) for comparison. Panel c) contains the SST differences between the NLOM solutions and the mooring.
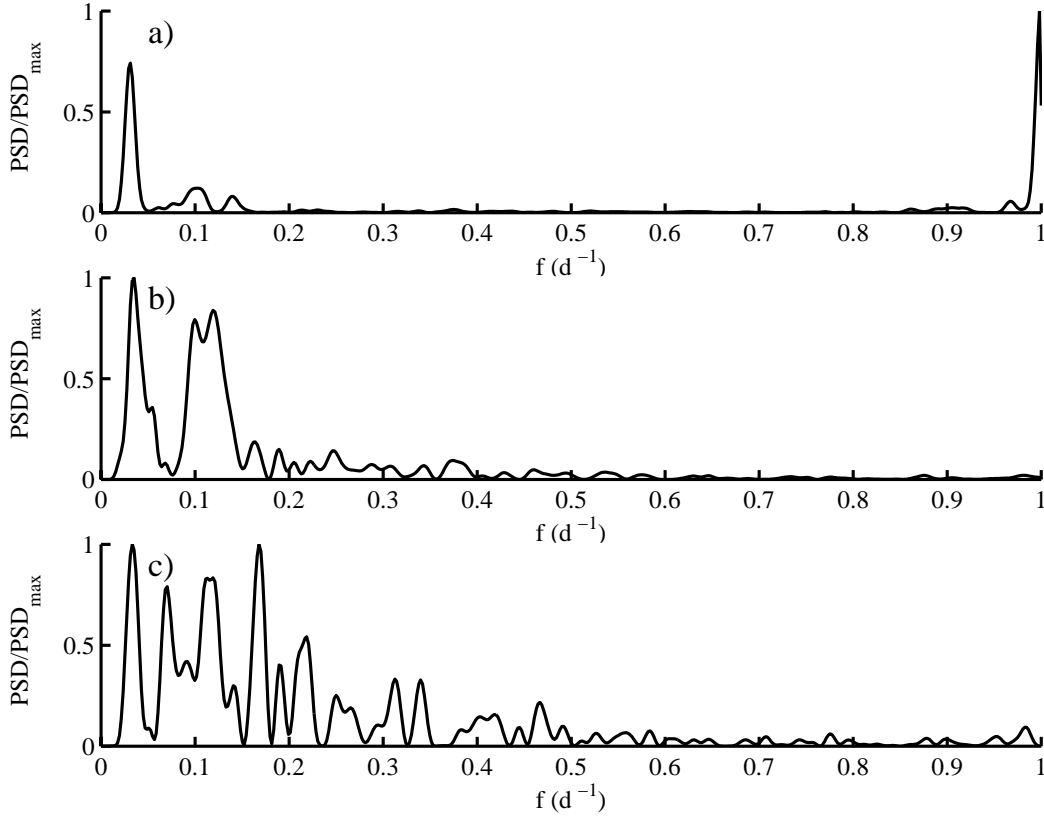
Fig. 4 — Power spectral density (PSD) of the mooring a) sea surface temperature (SST), b) mixed layer depth (MLD), and c) net surface heat fluxes (S. Flux) in reciprocal days (d^{-1}). A high-pass Butterworth filter has been applied to the 12-hourly averaged time series of these mooring observations to remove signals with periods greater than 40 days. The 40-day cycle at $f = 0.025\,d^{-1}$ is an artifact of the signal filtering, and the maximum frequency is $1\,d^{-1}$ because of the 12-hourly frequency. The PSD has been scaled by the maximum value for the frequency range (PSD_{max}).

Not surprisingly, the 12-hourly operational wind products are more successful in producing a model SST that follows the higher frequency variability in the mooring record. This is most noticeable in the double SST peak of April-May 1995, and in the earlier rise in SST during August-October 1995. The peak SST value in mid-October 1994 is also well reproduced, albeit a few days early. Of the operational wind experiments, the FNMOC yields the best SST agreement with the buoy as it has the smallest $|\Delta SST|$ (Fig. 3c) and the highest SST correlation (Table 8). We note the FNMOC and FNMOC 10 m experiments yielded SST solutions that are quite close to each other during the mooring observation period.

To provide a measure of the agreement between the model and buoy SST, we computed correlations between the time series (Table 8). They reveal that a comparable agreement is obtained between the model and buoy SST as between the climatological and buoy SST. The correlation between NLOM SST and buoy SST is noted to increase with the increase in value of skill score between the wind product and the mooring wind record (Table 5). The very high SST correlations are because the low-frequency seasonal cycle dominates the time series. The buoy-climatology correlation is the strongest because the higher frequency oscillations in the SST solutions from the operational wind experiments are out of phase with the oscillations in the buoy SST. The
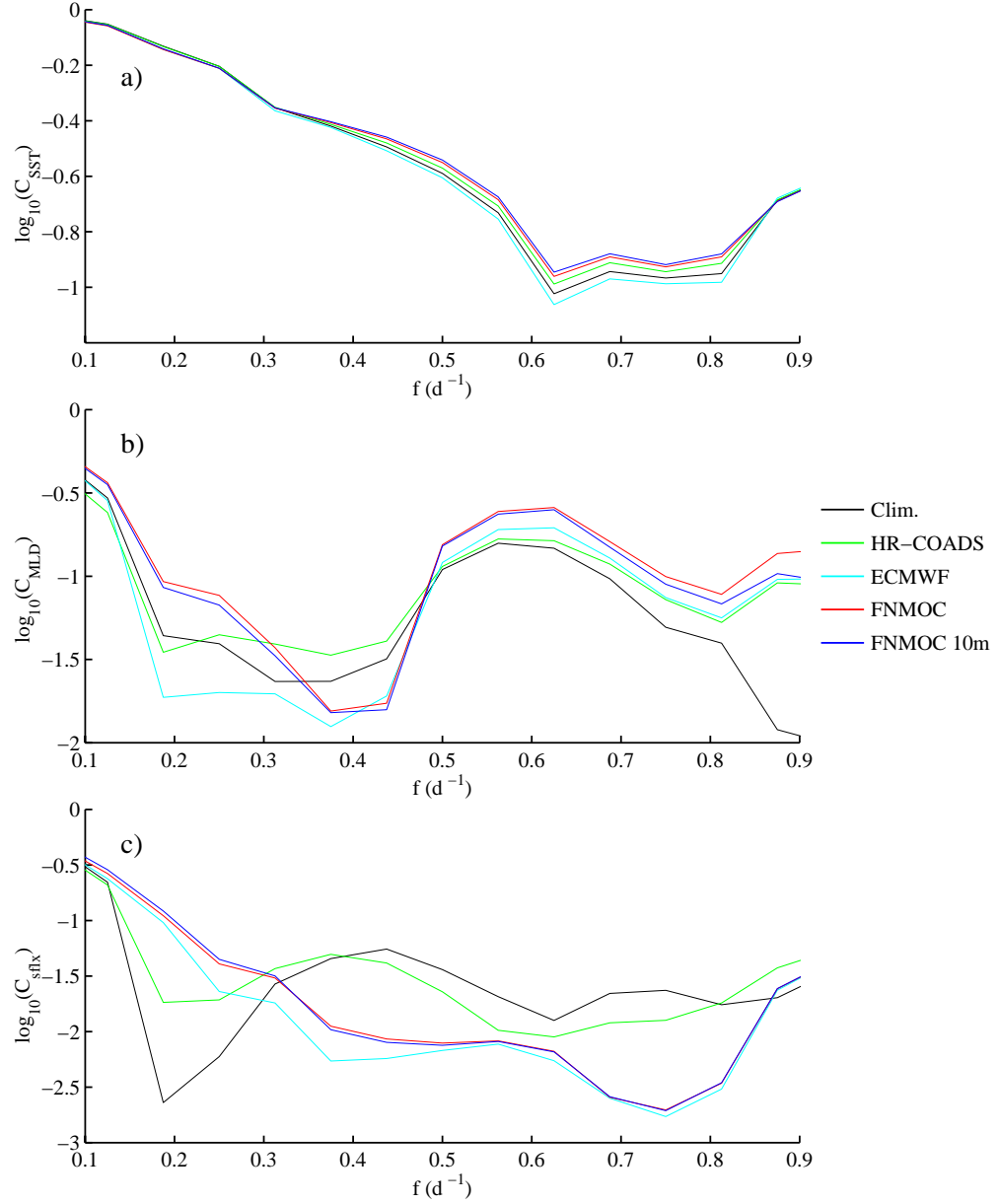
Fig. 5 — Coherency spectrum between the 12-hourly averaged buoy observations and time series from the four NLOM experiments: climatological winds (HR-COADS), ECMWF 1000 mb winds, FNMOC surface stresses and 10 m winds (FNMOC), and FNMOC 10 m winds (FNMOC 10m). The coherency spectrum between buoy and climatology (Clim.) is included for completeness. The coherence spectra are shown for a) SST (C_{SST}), b) MLD (C_{MLD}), and c) net surface heat fluxes (C_{sflx}), and were computed using a fast Fourier transform of length 32. A log scale is used to accentuate the differences at low coherence.

other significant frequencies can be determined from the power spectral density (PSD) of the buoy SST (Stoica and Moses 1997). After a 10th-order high-pass Butterworth filter has been applied to remove signals with periods greater than 40 days, the PSD determined with a Hanning window shows that the daily ($f = 1\,d^{-1}$) and 10-day ($f = 0.1\,d^{-1}$) variations are the next most important contributions (Fig. 4). By computing a coherency spectrum between the mooring record and the other time series (Fig. 5), it is seen the FNMOC experiment yields a NLOM-buoy SST correlation that is slightly better than the corresponding correlation from the HR-COADS experiment for time periods of 1.25 to 3 days, as expected for a twice-daily surface forcing.

The FNMOC SST solution is in closest agreement with the buoy SST because the FNMOC surface stresses and FNMOC 10 m winds follow the mooring record most closely (Figs. 1 and 2). The surface stresses follow the relaxation in winds in the mooring record quite well in late August, and the FNMOC 10 m winds have a deeper and narrower minimum in late July compared to the ECMWF winds. Specific time periods where the NLOM SST solutions agree well (and less well) with the buoy SST can also be directly related to the agreement between wind products and the mooring wind record. During periods when the wind product is weaker than the buoy wind observations (Fig. 1b), the model net surface heat flux is greater because the reduction in wind-speed dependent latent cooling increases the model SST relative to the buoy SST. The reverse is also true when the wind product is stronger than the buoy wind. Similarly, whenever the wind stresses are weaker than the buoy observations (Fig. 2b), the amount of cooling due to entrainment of cold water through wind stirring is decreased, thereby increasing the model SST.

It is noteworthy that although the ECWMF wind speeds are up to 50% stronger during the SW monsoon than the buoy winds, the SW monsoon ECMWF SST differs only slightly from the SST obtained using the other wind products. This is in stark contrast to the ECMWF SST being much lower than the SST from the other simulations during the NE monsoon. This reveals that different physical processes are responsible for the decrease in SST during the NE and SW monsoons.

We also note that the more pronounced monsoon relaxation and resurgence in the last week of July as depicted in the FNMOC wind products relative to the ECMWF wind products, did not produce any evidence of a narrow minimum or maximum in the FNMOC SST compared to the ECMWF SST. Given the success of the NLOM in capturing the SST double peak in the 1995

Table 8 — Time series correlations (r) of the monthly climatologies (Clim.) and model experiments (Expt.) with respect to the buoy observations (Buoy).

| Expt. | r(Expt.,Buoy) | | | r(Expt.,Clim.) | |
	r(SST,SST)	r(MLD,MLD)	r(Q,Q)	r(SST,T_a)	r(Q,Q)
Clim.	0.96	0.63	0.73	0.98	1.00
HR-COADS	0.89	0.40	0.64	0.94	0.80
ECMWF	0.90	0.65	0.56	0.94	0.70
FNMOC	0.93	0.84	0.61	0.94	0.71
FNMOC 10 m	0.92	0.77	0.65	0.95	0.76

spring intermonsoon, we conclude that dynamical processes other than just wind forcing must be responsible for the SST minimum that appears in the last week of July in the mooring record. One possibility is a short term and rapid change in the solar radiation, air temperature, and specific humidity, as the NLOM simulations have been forced with monthly climatologies of these quantities.

6. MIXED LAYER DEPTH

The buoy MLD used for comparison against the model MLD prediction is chosen as the depth at which the temperature has decreased by $0.1\,°C$ from the SST (Rudnick et al. 1997). For comparison we have also included a corresponding climatological MLD which we have inferred from the Levitus monthly temperature climatology (Levitus et al. 1994) for the same $0.1\,°C$ criteria. This climatological MLD fails to properly represent the seasonal MLD cycle indicated by the mooring observations. It indicates an actual shallowing of the MLD at the peak of the NE monsoon, and seriously underestimates the depth of the mixed layer during both monsoons. We've included it to merely illustrate the difficulty in validating OGCM mixed layer depths over basin scales against MLD climatologies.

The NLOM is less successful in simulating the mooring MLD than it is in simulating the mooring SST (Fig. 6), having differences of up to $60\,m$ during the NE and SW monsoons. The MLD correlations (Table 8) are lower because of the $20\,m$ minimum depth imposed within the model to maintain stability. This prevents the NLOM from reproducing the very shallow buoy MLD during the intermonsoon periods, and the 10-day oscillations that strongly dominate at high frequencies in the latter (Fig. 4).

The correlation for the HR-COADS MLD is noticeably poorer because the mixed layer continues to deepen during the second half of the SW monsoon when the buoy record indicates a shallowing. This is confirmed by calculating the correlations for just the NE and SW monsoon periods. For the NE monsoon, a significant correlation is found for the NLOM MLD with respect to the buoy MLD ($r = 0.74$), while a very poor correlation is obtained for the SW monsoon ($r = 0.05$).

The operational wind products are more successful at capturing the mixed layer deepening during the NE and SW monsoons. This is evidenced by their higher correlations (Table 5) due to their greater coherence at periods of 1.5 to 2 days (Fig. 5). All operational wind experiments yield a deeper MLD during the NE monsoon than the HR-COADS solution, and a shallower SW monsoon MLD that more closely tracks the mooring record (smaller $|\Delta MLD|$ in Fig. 6c). They are quite distinct in their NLOM MLD solutions during the SW monsoon, indicating the sensitivity of the MLD to the differences in the wind products. The FNMOC solution provides the best MLD prediction, in large part because it captures the MLD retreat in the second half of the SW monsoon as indicated in the mooring record. It is because of the large decrease in FNMOC surface wind stress to values in close agreement with the buoy in mid-August that the FNMOC MLD captures this retreat event.

The deeper FNMOC mixed layer during January 1995 relative to the ECMWF MLD is at odds with the increased surface heating one would expect from FNMOC $10\,m$ winds that are up to $2\,\mathrm{m\,s^{-1}}$ weaker than the ECMWF $1000\,mb$ winds (Fig. 1b). The deeper FNMOC mixed layer is due to increased net surface cooling that is made possible by a northwestward current advecting warm equatorial surface water to the mooring site (*cf* Section 9.1). This northwestward current is induced
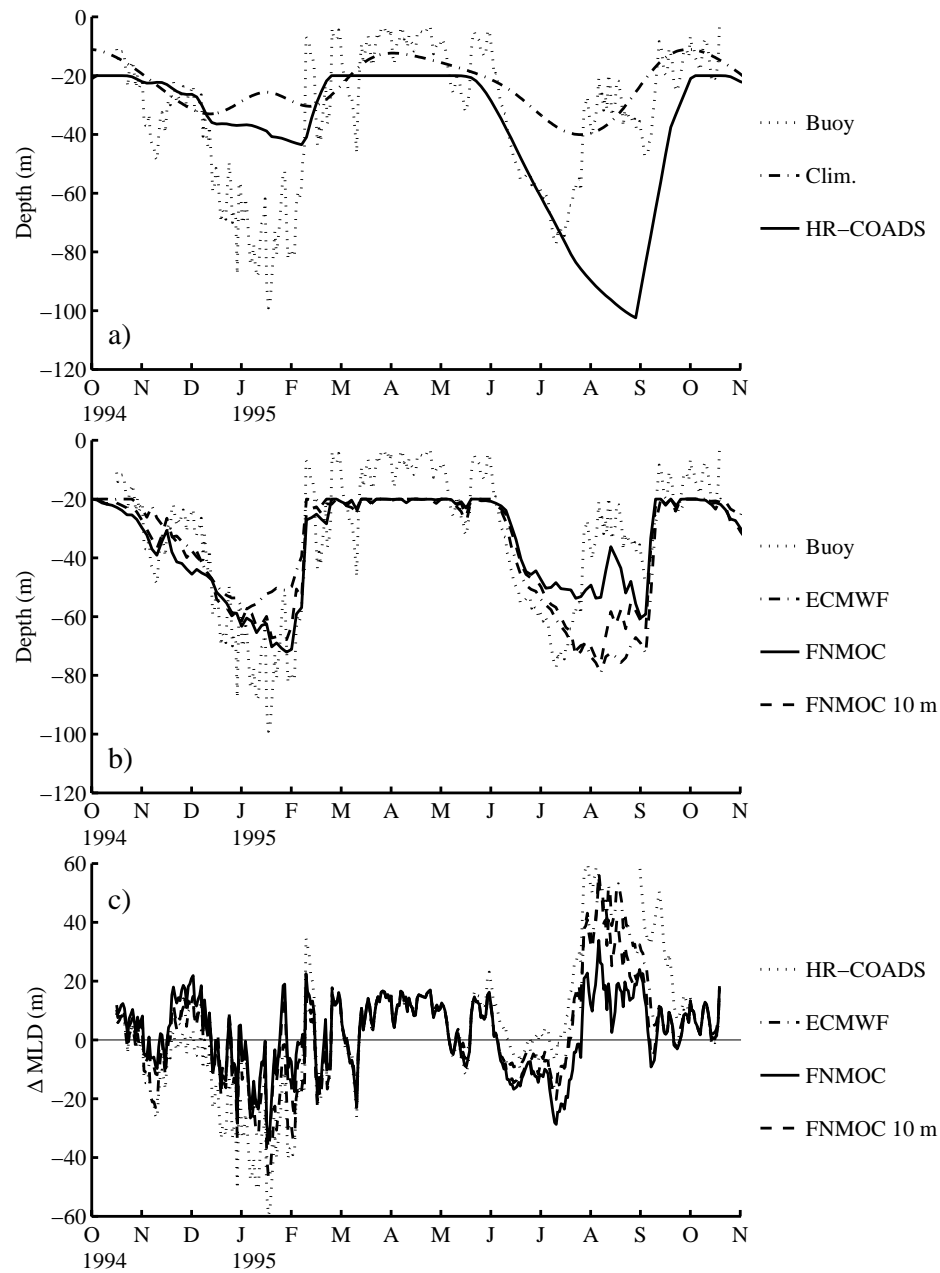
Fig. 6 — Time series of MLD from the four wind experiments: a) climatological winds (HR-COADS), b) ECMWF 1000 mb winds, FNMOC surface stresses and 10 m winds (FNMOC), and FNMOC 10 m winds (FNMOC 10m). The 0.1 °C MLD from the WHOI mooring (Buoy) and from the Levitus climatology (Levitus) are included in a) and b) for comparison. Panel c) contains the MLD differences between the NLOM solutions and the mooring.

in the first week of January by the FNMOC surface winds, as opposed to a northeastward current as obtained in the last 2 weeks of January with the ECMWF 1000 mb winds. This northwestward current brings more warm water to the mooring location, leading to a warmer model SST than in the ECMWF wind experiment. As a consequence, greater surface cooling occurs and a deeper mixed layer develops in our model. This dynamical response is due to model limitations in representing the surface heat fluxes and upper ocean turbulent mixing. The air temperature is prescribed to remain fixed when it would warm up in the prolonged presence of the warmer SST, thereby reducing the surface cooling. The contribution of horizontal advective heat fluxes is not included in the 1-D turbulent kinetic energy of the modified Kraus-Turner model. The inclusion of such a contribution would increase surface buoyancy and thereby inhibit mixed layer deepening.

Of the four numerical experiments, the FNMOC surface wind stress experiment best represents the observed MLD during the second half of the SW monsoon (Fig. 6). This is because the FNMOC surface stress best depicts the major relaxation of the SW monsoon during the mid-July to mid-August period. The stronger FNMOC 10 m and ECMWF 1000 mb wind stresses during the second half of the SW monsoon are responsible for the deeper mixed layer at this time.

7. CURRENTS

The mooring record shows the influence of strong flows associated with mesoscale geostrophic features because of the strong influence of eddy activity at the mooring site (Weller 1999). As a consequence, the NLOM layer 1 currents do not accurately represent the corresponding mooring layer 1 averages (Fig. 7) formed from the time series of mooring subsurface currents and layer 1 thicknesses (Fig. 8). Accurately predicting currents at a fixed location in a region of strong eddy variability, such as the Arabian Sea, has traditionally been a difficult challenge for all OGCMs. While the model is able to represent the more deterministic boundary currents, an accurate depiction of the mesoscale variability in the interior of the Arabian Sea would require higher horizontal resolution (1/8° or better) and the assimilation of satellite-inferred SST and sea surface height (SSH) data into the model. Studies have demonstrated the increased model skill at hindcasting mesoscale eddies and meandering frontal structure in nondeterministic regions when assimilating satellite-inferred SSH into the NLOM (Smedstad et al. 1994, Smedstad et al. 1997, Hurlburt et al. 1996). The improvements are smaller in equatorial regions where the ocean has a strong deterministic response to wind forcing. NLOM studies have also shown the importance of having high horizontal resolution and upper ocean-topographical coupling via baroclinic instability, in order to properly resolve the eddy scales (Hurlburt et al. 1996, Hogan and Hurlburt 2000). Including realistic bottom topography via the finite-depth formulation of the NLOM would therefore aid in this regard. Implementing these features is beyond the scope of the present study.

8. SURFACE HEAT FLUXES

The NLOM heat fluxes (Fig. 9) agree more poorly with respect to the buoy than the climatological heat fluxes (Table 5). The operational wind solutions perform more poorly than the buoy and climatological solutions because they have negligible coherence for 2 to 3 day oscillations (Fig. 5), even though they perform better than climatology and the NLOM HR-COADS solution for 5-day oscillations. This is because the PSD for the buoy surface heat fluxes occupies a larger range of higher frequencies, and has a local minimum at 5-day oscillations ($f = 0.2\,d^{-1}$, Fig. 4). The lack of better coherence with increasing frequency for the NLOM solutions points to the importance of
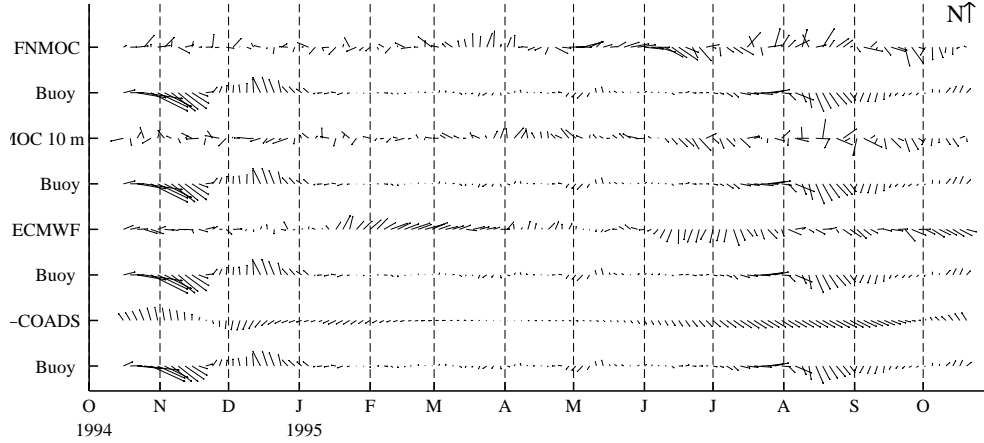
Fig. 7 — Time series of the NLOM layer 1 currents at the WHOI mooring location (61.5°E, 15.5°N) for the four wind experiments: climatological winds (HR-COADS), ECMWF 1000 mb winds (ECMWF), FNMOC surface and 10 m winds (FNMOC), and only FNMOC 10 m winds (FNMOC 10m). The lengths of the sticks correspond to magnitude. Northward and eastward flow are in the upward and rightward directions, respectively.

other factors in addition to wind speed for predicting surface heat fluxes, e.g. higher frequency air temperatures and net surface radiation.

The low heat fluxes of the spring intermonsoon (Fig. 9) coincide with the mixed layer depth shallowing to the imposed minimum value (Fig. 6). The model assumes complete absorption of solar radiation heating within the mixed layer, and neglects the solar heating that could occur beneath the mixed layer when light penetrates to greater depths under optically clear conditions. This neglect could produce excessive SST warming when the mixed layer is at its minimum depth, thereby producing low NLOM heat fluxes because of excessive latent cooling. Allowing for a depth-dependent solar radiation profile is expected to improve the agreement between the NLOM and buoy surface heat fluxes. The excessive surface heating by the model during the SW monsoon is because of the too-cold SST during this time and is due to the large temperature difference imposed at the base of the mixed layer (*cf* Section 5).

A remarkable outcome is that the same annual cycle occurs for the surface heat fluxes despite the major differences in the wind forcing (Fig. 9c). This suggests the SST is relaxing towards the COADS surface air temperature in a manner indicative of a Haney-type boundary condition (Haney 1971). To test the conjecture, correlations were computed between model SST and COADS air temperature, and between the model and climatological net heat flux (Table 5). The $r(SST, T_a)$ values all show large constant correlations (0.94-0.95) that are comparable to the correlation between the SST and air temperature from COADS (0.98). The $r(Q, Q)$ correlations of the model net heat fluxes with respect to COADS are appreciably smaller (0.70-0.80), and are comparable to the correlation between the COADS and buoy net heat fluxes (0.73). If SST is a consequence of the net heat fluxes applied at the surface, a larger variation in $r(SST, T_a)$ values would occur that follows the variation in $r(Q, Q)$ correlations. The absence of this relationship supports our conjecture that our heat flux forcing is relaxing the model SST towards the prescribed air temperature.

This relaxation becomes evident when the heat flux term in the SST equation is expanded
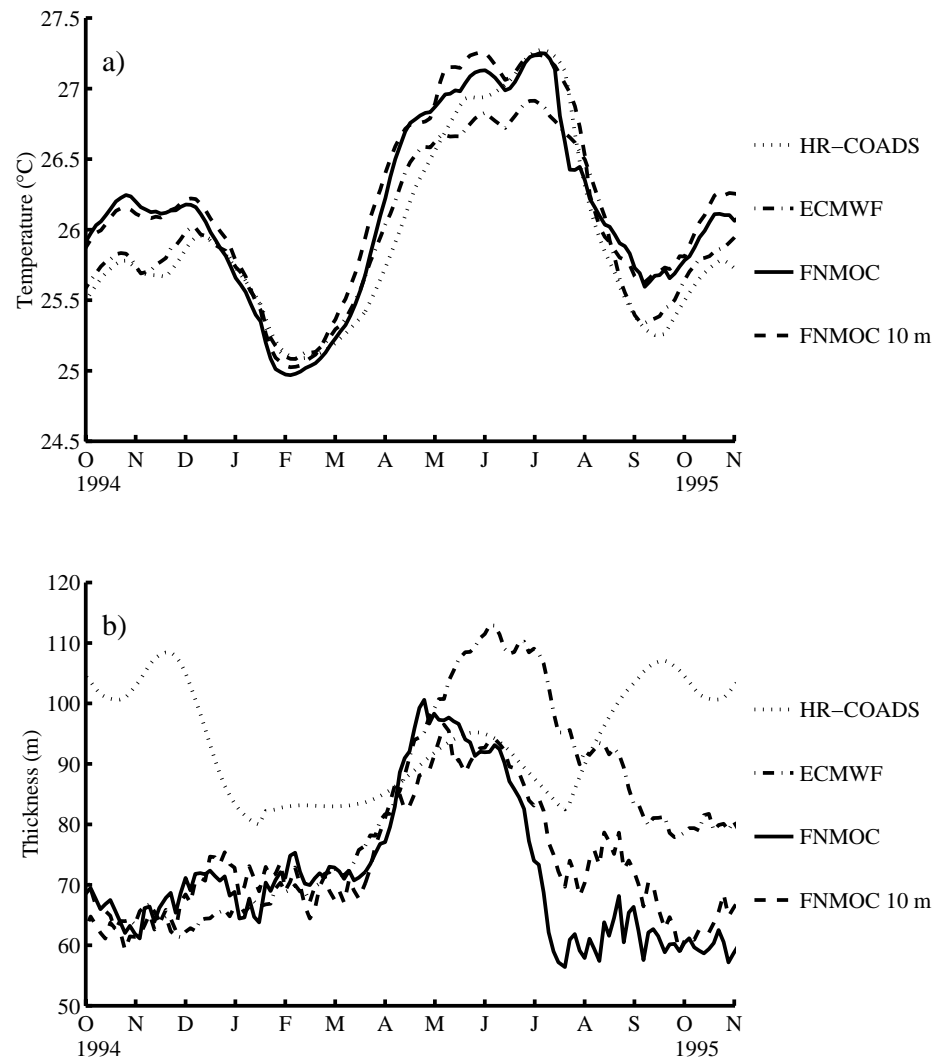
Fig. 8 — Time series of a) layer 1 temperature and b) layer 1 thickness from the four wind experiments: climatological winds (HR-COADS), ECMWF 1000 mb winds, FNMOC surface stresses and 10 m winds (FNMOC), and FNMOC 10 m winds (FNMOC 10m).
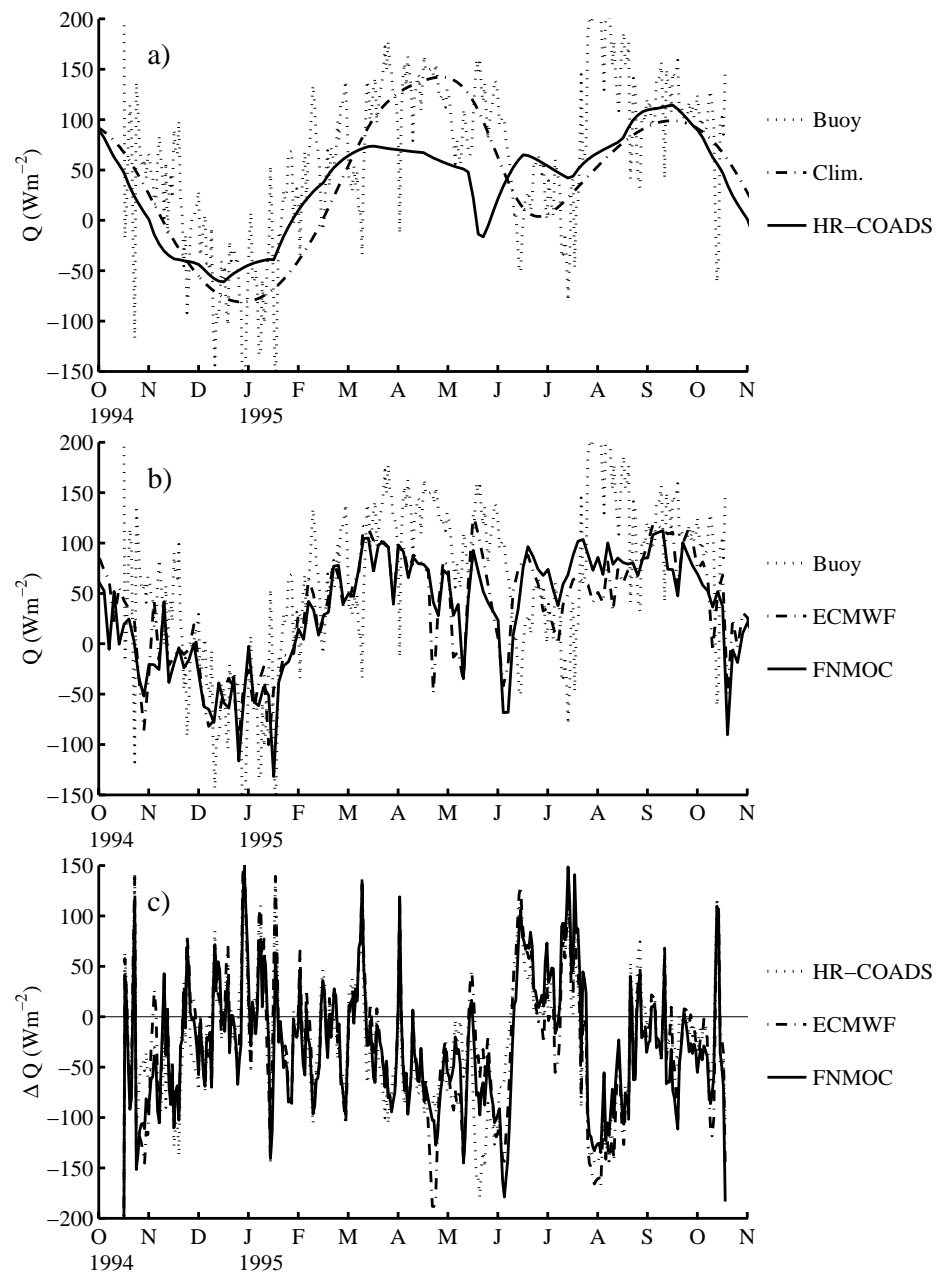
Fig. 9 — Time series of net surface heat fluxes from the four wind experiments: a) climatological winds (HR-COADS), b) ECMWF 1000 mb winds, FNMOC surface stresses and 10 m winds (FNMOC), and FNMOC 10 m winds (FNMOC 10m). Net surface heat fluxes from the WHOI mooring (Buoy) and the COADS climatology (COADS) are included for comparison. Panel c) contains the heat flux differences between the NLOM solutions and the mooring.

into its components (Section 3.2). A linear relaxation of the model SST to the air temperature is introduced via the sensible heat flux. The latent heat flux introduces a nonlinear relaxation between the model SST and the air temperature through the humidity difference. Because there is no change in T_a and q_a in response to the thermal state of the ocean, i.e., no air-sea feedback mechanism, the NLOM SST relaxes towards an equilibrium state that is offset from the air temperature. As a consequence, the net surface heat fluxes follow a repeatable annual cycle that deviates only when there are large changes in the ocean model MLD and SST. This is consistent with the findings of other authors (Seager et al. 1988, Seager and Blumenthal 1994) who argue that specifying the air temperature and humidity in the heat flux boundary conditions of an OGCM is equivalent to imposing the SST. This is a constraining feature of this surface heat flux forcing. However, it is the best heat flux formulation that can be implemented using monthly mean atmospheric fields. Better formulations that include the effects of atmospheric stability (Fairall et al. 1996, Seager et al. 1995) require forcing the NLOM with atmospheric fields that vary on time scales of 24 hours or less, or fully coupling the NLOM to an atmospheric general circulation model.

9. LAYER HEAT BALANCES

To determine the relative importance of the different heating mechanisms in influencing SST and MLD, we perform here an analysis of the heat balances within the mixed layer and the uppermost dynamical layer of the NLOM. In particular, we attempt to address the importance of two mechanisms for influencing the SST during the 1994 NE and 1995 SW monsoons. The first is how variations in surface wind stress can cool SST through entrainment of deeper colder water via wind stirring. The second is how changes in the wind driven currents may influence SST via heat advection. We include a heat balance analysis of the first layer to confirm the findings of the heat balance analysis for the mixed layer, and to explain changes in the heat balance that occur when the mixed layer and layer 1 have merged. The four different heat balance terms due to surface heating, advection, interlayer mixing, and diffusion are defined in Appendix C.

Although the model does not represent the eddy-dominant velocity field observed at the buoy location, we use the model circulation to examine the potential role of the basin-wide background circulation in the upper ocean heat balances. While it is possible to compute layer-average horizontal heat advection from the mooring observations to compare against the NLOM, we have chosen to omit it until the model also includes the assimilation of satellite observations to better depict the effects of mesoscale variability. The heat fluxes from the FNMOC 10 m solution are not shown because, aside from the horizontal advection contribution, they are essentially the same as the FNMOC solution.

9.1 Mixed Layer Heat Balances

The heat fluxes for the mixed layer (Fig. 10) show that appreciable horizontal (H. Adv.) and vertical (V. Adv.) advective cooling occurs from late in the spring intermonsoon (early May) to near the end of the SW monsoon (early September), in counter balance to the heating provided by the surface heat fluxes. The constraining influence of global detrainment $(\Omega_k \widehat{\omega}_k)$ on mixed layer deepening is responsible for the decrease in vertical advective cooling when the mixed layer and layer 1 have merged in early July. Vertical advective cooling ceases completely when the mixed layer undergoes retreat in late August. The appearance of the intense Findlater Jet (Figs. 1 and 2) is responsible for the offshore advection of water along the Oman coast and the consequent upwelling

of cold water. It is the arrival of this advected cold water at the mooring (Fig. 11) that is responsible for the change in early July from small heating to strong cooling in the horizontal advective heat flux. There is little heat flux from diffusion because the approximately uniform NLOM SST and MLD produce very weak horizontal gradients.

The stronger advective heating and cooling events during the NE and SW monsoons in the operational wind experiments are a consequence of the larger changes in the current circulation induced by these winds (Fig. 7). With the ECMWF winds, the horizontal advective cooling is twice as strong in the 1994 SW monsoon as in the 1995 SW monsoon. This is due to a weakening in the 1995 SW monsoon ECMWF winds relative to 1994, which gives rise to diminished advective cooling because of a weaker current and shallower MLD. The ECMWF horizontal advective cooling in the 1995 SW monsoon is greater than in the FNMOC and FNMOC 10 m wind experiments because of the more steady eastward current produced in August by the ECMWF winds (Fig. 7). All operational wind products display advective heating during the 1994 NE monsoon, with the FNMOC solution being the strongest, in contrast to the negligible contribution obtained with the HR-COADS winds.

The average and integrated mixed layer heat balances over the NE and SW monsoons (Table 9) reveal that the decrease in SST during the NE monsoon in the wind experiments is due to both surface cooling and vertical advective cooling produced by the combination of wind stirring and negative buoyancy. During the SW monsoon, vertical advective cooling is responsible for the decrease in SST, with the significant horizontal advective heat flux in the second half of the SW monsoon making a secondary contribution of up to as much as one-third. This strong cooling from entrainment is offset by the large surface heating. The monsoon averages for the net surface heat flux from the model are consistent with mean values calculated from the buoy observations (Weller et al. 1998). The model removes more heat from the ocean during the NE monsoon than buoy measurements indicate, and contributes less heat to the ocean over the SW monsoon than recorded by the buoy. Note the sum of the model heat fluxes remove almost twice as much heat energy from the ocean at the mooring location over the SW monsoon than over the NE monsoon.

9.2 Surface Dynamical Layer

The heat fluxes obtained for layer 1 for the various experiments (Fig. 12) are in consistent agreement with those obtained for the mixed layer heat fluxes (Fig. 10). Significant heat balance contributions occur for all terms but diffusion (Fig. 12). Diffusive cooling is larger here than within the mixed layer (Fig. 10) because of the greater spatial variability in layer 1 thickness. The heat changes due to advection events make the strongest contributions in the heat balances. For example, for the climatological solution (Fig. 12a) the peak advective cooling in layer 1 is twice as large as the peak advective cooling in the mixed layer. This cooling occurs because of the sharp temperature fronts of layer 1 created when cold water from layer 2 is entrained into layer 1. Clearly, the advective heat fluxes are sensitive to changes in the basin scale circulation. This is evident from the operational wind experiments, where significant heating and cooling advection events for layer 1 are found to occur (Fig. 12b-c) for which there is no mixed layer equivalent. These strong advective events correlate with the changes in layer 1 temperature and thickness (Fig. 8), and are attributed to geostrophic flow. For example, in the ECMWF case (Fig. 8b), the layer 1 thickness remains approximately constant during the October-November time period as compared to the more rapid variation in the climatological wind experiment (Fig. 8a). This
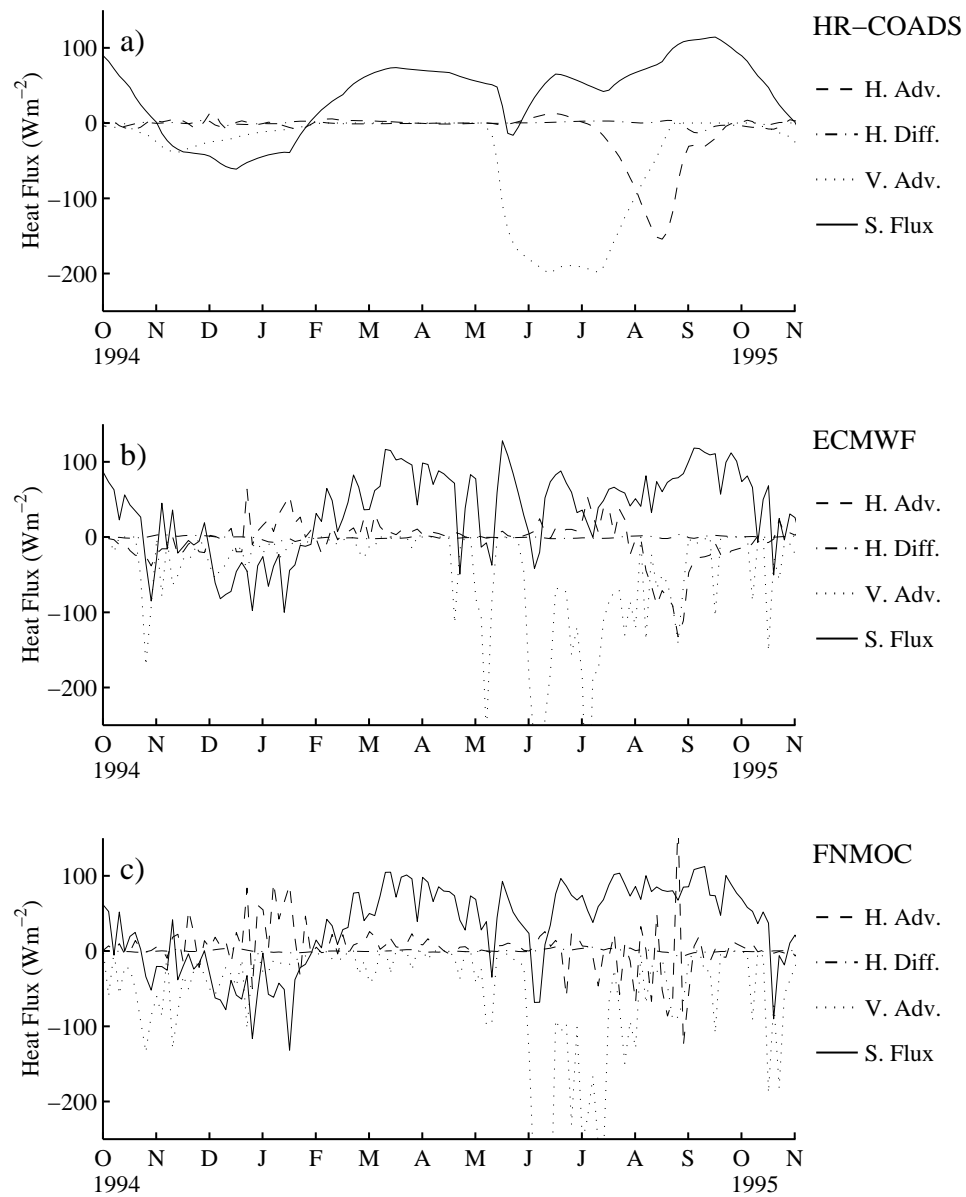
Fig. 10 — Time series of heat fluxes within the mixed layer for years 1994-1995 from the four wind experiments: climatological winds (Clim.), ECMWF 1000 mb winds, FNMOC surface stresses and 10 m winds (FNMOC), and FNMOC 10 m winds (FNMOC 10m). The layer heat fluxes shown are the contributions due to horizontal advection (H. Adv.), horizontal diffusion (H. Diff.), vertical advection (V. Adv.), and net surface heat fluxes (S. Flux).

Table 9 — Shown for the different experiments (Expt.) are the various heat fluxes for the mixed layer: advection (Adv), diffusion (Diff), layer mixing (LMix), net surface heat fluxes (Sflx), and the net heat flux from their sum (Net). The first row (Buoy) lists the net surface heat flux values from Weller et al. (1998) for comparison.

| Expt.	H.F.	NE Monsoon		SW Monsoon	
		Ave. H.F. $(\mathrm{W\,m^{-2}})$	Int. H.F. $(\mathrm{MJ\,m^{-2}})$	Ave. H.F. $(\mathrm{W\,m^{-2}})$	Int. H.F. $(\mathrm{MJ\,m^{-2}})$
Buoy	Sflx	-19.7	-182.12	89.5	827.41
HR-COADS	Adv	0.21	1.89	-41.28	-391.57
	Diff	-0.18	-1.62	0.01	0.09
	LMix	-16.07	-143.96	-118.83	-1127.29
	Sflx	-29.97	-268.56	69.60	660.25
	Tot	-46.01	-412.24	-90.50	-858.52
ECMWF	Adv	1.53	13.72	-13.72	-130.13
	Diff	-0.49	-4.36	-0.49	-4.64
	LMix	-25.75	-230.68	-115.52	-1095.91
	Sflx	-24.79	-222.07	56.15	532.67
	Tot	-49.49	-443.39	-73.58	-698.01
FNMOC	Adv	17.69	158.54	-7.36	-69.85
	Diff	0.81	7.30	0.80	7.56
	LMix	-36.82	-329.85	-124.18	-1178.04
	Sflx	-24.47	-219.21	66.80	633.70
	Tot	-42.77	-383.23	-63.95	-606.63
FNMOC 10 m	Adv	10.92	97.85	-40.68	-385.89
	Diff	1.88	16.88	0.65	6.17
	LMix	-34.69	-310.82	-117.36	-1113.35
	Sflx	-20.12	-180.31	66.63	632.11
	Tot	-42.01	-376.40	-90.75	-860.96
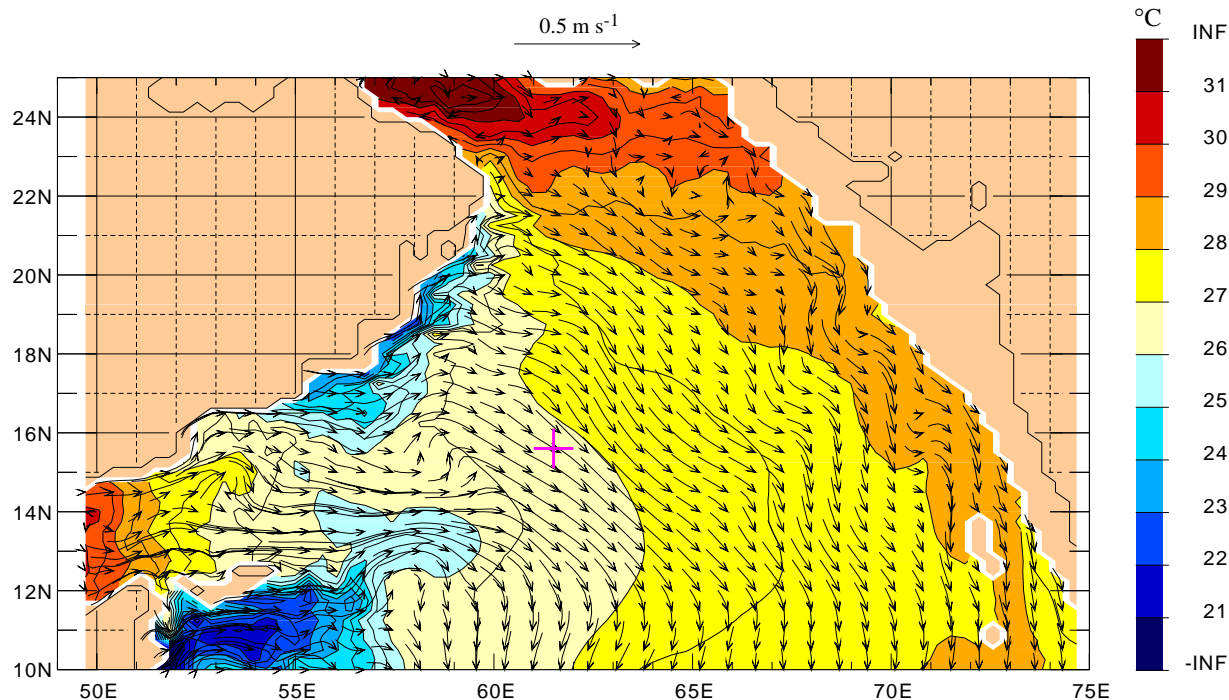
Fig. 11 — The SST and surface currents predicted for the Arabian Sea basin by the NLOM wind climatology experiment (HR-COADS) for Julian day 191 (July 10). The location of the WHOI mooring at (61.5°E, 15.5°N) is indicated by the pink cross. Clearly evident are the colder surface waters along Oman and south of Socotra produced by coastal upwelling of deeper water. The advection of the Oman coastal water to the mooring is partially responsible for cooling the mixed layer at this location in mid-July.

produces a much weaker geostrophic flow and hence a considerably diminished advective heat flux. Given that the transport in the NLOM is directly proportional to the gradient in layer temperature and thickness, it is not surprising that advective heat fluxes correlate with the layer 1 temperatures and thicknesses.

As expected, entrainment cooling of the mixed layer only occurs during the brief time the mixed layer has merged with layer 1. It contributes much less towards the cooling of the layer as advection. This is in contrast to the mixed layer case where entrainment cooling dominates throughout the period of deepening due to wind stirring.

Advection and entrainment are responsible for cooling layer 1 during the SW monsoon. The heat input over the SW monsoon from the surface fluxes is approximately balanced by the heat removed by these processes. The cooling of layer 1 during the NE monsoon occurs because of surface cooling. The surface heat flux is responsible for the net heating at the mooring location over the course of the year.

10. SUMMARY AND CONCLUSION

In this report we investigate the sensitivity of mixed layer properties in the Arabian Sea to winds by using an OGCM forced with different wind products to interpret a one-year record of mooring observations. This was done to achieve a three-fold goal. First, to determine the sensitivity of the mixed layer in the Arabian Sea to variations in the winds. Second, to identify the origin of
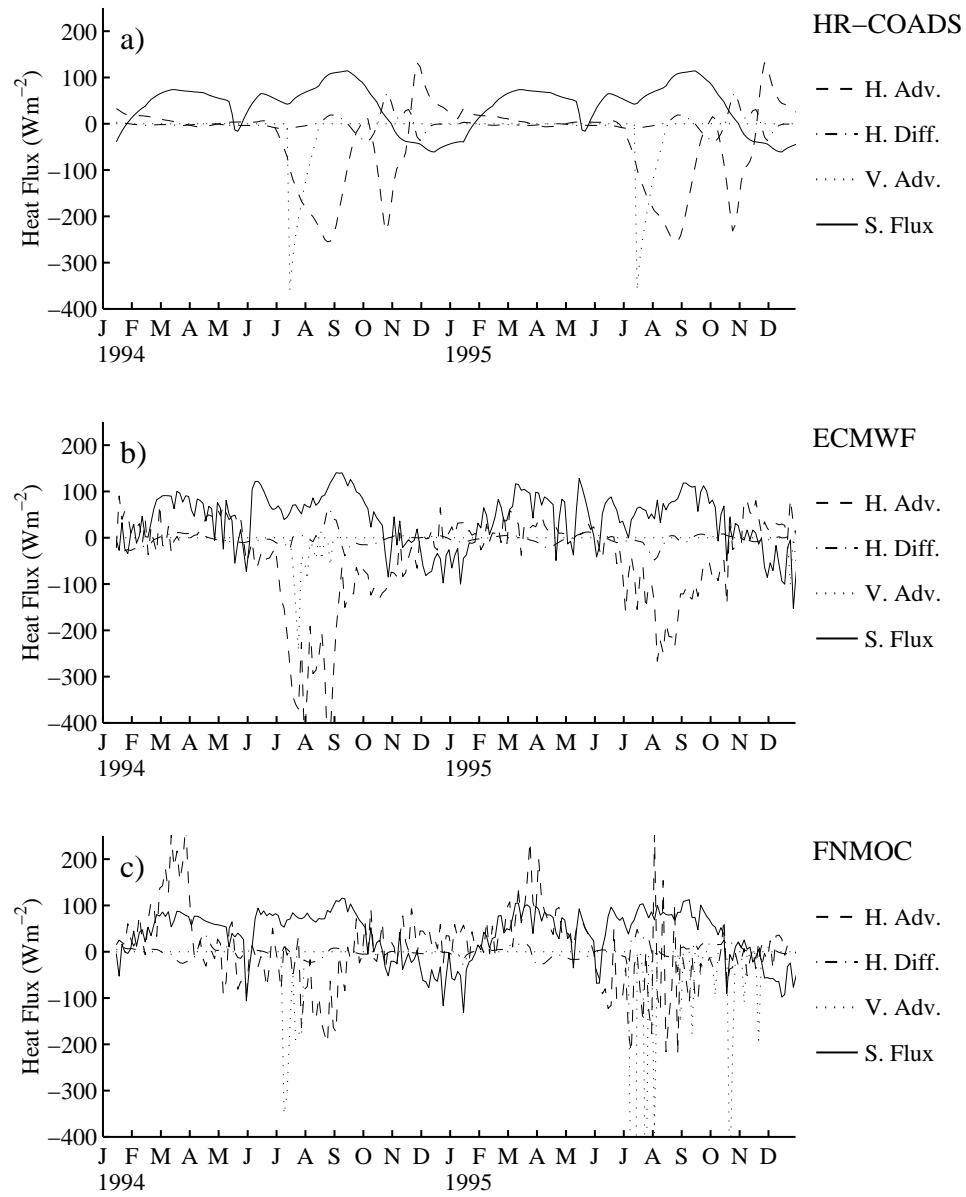
Fig. 12 — Time series of heat fluxes within layer 1 for years 1994-1995 from the four wind experiments. Refer to the caption of Fig. 10 for explanation of the labels.

mesoscale features and help interpret how they are responsible for features observed in the mooring record. Third, to determine which wind product works best as forcing for an OGCM when seeking to predict mixed layer properties. These goals were achieved by carrying out NLOM simulations using wind products from monthly mean climatologies (HR and COADS) and operational weather forecast models (ECMWF and FNMOC).

We found that both SST and MLD prediction in an OGCM are sensitive to variations in the wind stress magnitude, and to a lesser extent the wind speed dependence in the surface heat fluxes. The ability of an OGCM, in this case the NLOM, to reproduce the mooring record of SST and MLD is directly related to how closely the wind product used to construct the surface fluxes for the model agreed with the observed wind stress and wind speed.

Despite the failure of the NLOM to reproduce the current variability at the mooring location, this study uncovered a significant result. The large surface cooling observed in the mooring record during the NE monsoon is made possible in part by a northwestward current horizontally advecting warm water to the mooring location. Were it not for this advection, the SST would decrease more than is observed and thereby diminish the amount of surface cooling as directly seen in the ECMWF wind experiment.

Of the wind products considered, the FNMOC surface wind stresses and FNMOC 10 m wind speeds had the strongest correlations with the mooring wind record, and therefore yielded the best agreement between the NLOM predictions and mooring record for SST and MLD. This is because the surface stresses included the effects of atmospheric dynamic stability, and the 10 m winds were at a constant reference height. The ECMWF 1000 mb wind stresses performed more poorly because these effects were ignored (a constant drag coefficient was used) and because no consideration was given to the height varying 1000 mb surface. The ECMWF 10 m winds were not used in this study to form the wind stresses because in our earlier experience we found them to have serious bias problems. Our success with the FNMOC wind products indicates the importance of including atmospheric dynamic stability when constructing surface fluxes for use with an OGCM having an embedded mixed layer.

While this Indian Ocean NLOM has shown good skill at reproducing the mooring observations for SST and MLD, it is clearly deficient at predicting the currents and needs improvement in the surface heat fluxes. As we discuss in Section 7, to improve upon the basin scale circulation it will be necessary to increase the horizontal resolution of the model to at least 1/8° so that the NLOM will be sufficiently eddy-resolving. Moreover, the finite-depth version will need to be implemented to take full account of the coupling between the wind-driven surface currents and the topography-driven abyssal currents, as revealed from other NLOM studies. Reformulating the model to allow for a "floating" mixed layer that can penetrate beneath the first layer interface would also be a major improvement. This reformulation would reduce the increase in geostrophic flow that occurs during the SW monsoon, when the first layer interface is deepened by the mixed layer, and thereby improve the layer 1 currents. This would also remove artifacts that appear in the model SST and MLD as a consequence of constraining the mixed layer to within the first layer. A "floating" mixed layer has already been implemented in global version of the NLOM and is presently being evaluated.

Immediate improvement in the surface heat fluxes can be gained by using 12-hourly heat fluxes that include the effects of atmospheric stability. This can be achieved by using operational products and air-sea temperature dependent exchange coefficients in the NLOM surface heat flux forcing.

Given that the surface heat flux forcing applied here for the NLOM wind experiments is found to cause the model SST to relax towards an equilibrium state prescribed by the air temperature and humidity climatologies, it is reasonable to expect much better NLOM predictions of the SST. While this is inadequate if one's interest is simulating SST for climate studies, it serves well for an SST forecast model, such as the NLOM, that is used to support Navy Fleet operations.

11. ACKNOWLEDGMENTS

12. REFERENCES

Blackadar, A.K. and H. Tennekes, 1968: Asymptotic similarity in neutral planetary boundary layers, *J. Atmos. Sci.,* **25,** 1015–1020.

Bruce, J.G., D.R. Johnson, and J.C. Kindle, 1994: Evidence for eddy formation in the eastern Arabian Sea during the northeast monsoon, *J. Geophys. Res.,* **99,** 7651–7664.

Chu, P.C., Y. Chen, and S. Lu, 1998: On Haney-type surface thermal boundary conditions for ocean circulation models, *J. Geophys. Res.,* **28,** 890–901.

da Silva, A.M., C.C. Young, and S. Levitus, 1994: Atlas of surface marine data 1994. Volume 1: Algorithms and procedures. *NOAA Atlas NESDIS 6,* U.S. Department of Commerce, Washington, D.C.

ECMWF Research Department, 1998: ECMWF forecast model, adiabatic part, 2nd edition, European Centre for Medium Range Weather Forecasts, Reading, England.

ECMWF Research Department, 1991: ECMWF forecast model, physical parameterisation, 3rd edition, European Centre for Medium Range Weather Forecasts, Reading, England.

ECMWF Technical Attachment, 1993: The description of the ECMWF/WCRP Level III – A global atmospheric data archive European Centre for Medium Range Weather Forecasts, Reading, England.

Fairall, C.W., E.F. Bradley, D.P. Rogers, J.B. Edson, and G.S. Young, 1996: Bulk parameterization of air-sea fluxes for Tropical Ocean-Global Atmosphere Coupled-Ocean Atmosphere Response Experiment, *J. Geophys. Res.,* **101,** 3747–3764.

Gallacher, P.C., 1994: Air-sea feedback during coastal upwelling, in *Second International Conference on Air-Sea Interaction and Meteorology and Oceanography of the Coastal Zone*, American Meteorological Society, Lisbon, Portugal.

Gallacher, P.C., and G. Peggion, 1999: Air-sea feedback during coastal upwelling, *J. Phys. Oceanogr.,* submitted.

Gallacher, P.C., and P.A. Rochford, 1995: Numerical simulations of the Arabian Sea using tracers as proxies for phytoplankton biomass, *J. Geophys. Res.,* **100**, 18,565–18,579.

Garwood, R.W., 1977: An oceanic mixed layer model capable of simulating cyclic states, *J. Phys. Oceanogr.,* **7,** 455–468.

Garwood, R.W., P.C. Gallacher, and P. Muller, 1985: Wind direction and equilibrium mixed layer depth: general theory, *J. Phys. Oceanogr.,* **15**, 1325–1331.

Greenhut, G.K., and S.J.S. Khaksa, 1995: Bulk transfer coefficients and dissipation-derived fluxes in low wind speed conditions over the western equatorial Pacific Ocean, *J. Geophys. Res.,* **100,** 857–863.

Haney, R.L., 1971: Surface thermal boundary condition for ocean circulation models, *J. Phys. Oceanogr.,* **1,** 241–248.

Hellerman, S., and M. Rosenstein, 1983: Normal monthly wind stress over the world ocean with error estimates, *J. Phys. Oceanogr.,* **13,** 1093–1104.

Hogan, P.J., and H.E. Hurlburt, 2000: Impact of upper ocean-topographical coupling and isopycnal outcropping in Japan/East Sea models with 1/8° to 1/64° resolution, *J. Phys. Oceanogr.,* in press for September.

Hogan, T.F., and T.E. Rosmond, 1991: The description of the Navy operational global atmospheric prediction system's spectral forecast model, *Mon. Wea. Rev.,* **119,** 1786–1815.

Hurlburt, H.E., A.J. Wallcraft, W.J. Schmitz Jr., P.J. Hogan, and E.J. Metzger, 1996: Dynamics of the Kurosio/Oyashio current system using eddy-resolving models of the North Pacific Ocean, *J. Geophys. Res.,* **101,** 941–976.

Keen, T.R., J.C. Kindle, and D.K. Young, 1997: The interaction of southwest monsoon upwelling, advection and primary production in the northwest Arabian Sea, *J. Mar. Sys.,* **13,** 61–82.

Kindle, J.C., 1991: Topographic effects on the seasonal circulation of the Indian Ocean, *J. Geophys. Res.,* **96,** 16,827–16,837.

Kraus, E.B., and J.S. Turner, 1967: A one-dimensional model of the seasonal thermocline, II. The general theory and its consequences, *Tellus,* **19,** 98–106.

Levitus, S., 1982: Climatological Atlas of the World Ocean, *NOAA Prof. Pap. 13*, U.S. Govt. Print. Off., Washington, D.C.

Levitus, S., R. Burgett, and T.P. Boyer, 1994: World Ocean Atlas 1994. Volume 3: Salinity. *NOAA Atlas NESDIS 3*, U.S. Department of Commerce, Washington, D.C.

Levitus, S. and T.P. Boyer, 1994a: World Ocean Atlas 1994. Volume 4: Temperature. *NOAA Atlas NESDIS 4*, U.S. Department of Commerce, Washington, D.C.

Levitus, S. and T.P. Boyer, 1994b: World Ocean Atlas 1994. Volume 2: Oxygen. *NOAA Atlas NESDIS 2*, U.S. Department of Commerce, Washington, D.C.

McCreary, J.P., and P.K. Kundu, 1989: A numerical investigation of sea surface temperature variability in the Arabian Sea, *J. Geophys. Res.*, **94,** 16,097–16,114.

McCreary, J.P., P.K. Kundu, and R.L. Molinari, 1993: A numerical investigation of dynamics, thermodynamics, and mixed-layer processes in the Indian Ocean, *Prog. Oceanogr.*, **31,** 181–244.

Metzger, E.J., and H.E. Hurlburt, 1996: Coupled dynamics of the South China Sea, the Sulu Sea, and the Pacific Ocean, *J. Geophys. Res.*, **101,** 12,331–12,352.

Millero, F.J. and A. Poisson, 1981: International one-atmosphere equation of state of seawater, *Deep Sea Res., Part A*, **28**, 625–629.

Murphy, A.H., 1995: Skill scores based on the mean square error and their relationships to the correlation coefficient. *Mon. Wea. Rev.*, **116**, 2417–2424.

Niiler, P.P., and E.B. Kraus, 1977: One-dimensional models of the upper ocean, in *Modeling and Prediction of the Upper Layers of the Ocean,* E.B. Kraus, ed., Pergamon Press, New York.

Rao, R.R., R.L. Molinari, and J.F. Festa, 1989: Evolution of the climatological near-surface thermal structure of the tropical Indian Ocean. Part 1: Description of mean monthly mixed layer depth, and sea surface temperature, surface current, and surface meteorological fields, *J. Geophys. Res.*, **94,** 10,801–10,815.

Rudnick, D.L., R.A. Weller, C.C. Eriksen, T.D. Dickey, J. Marra, and C. Langdon, 1997: Moored instruments weather Arabian Sea monsoons, *EOS*, **78**, 117.

Seager, R., and M.B. Blumenthal, 1994: Modeling tropical Pacific sea surface temperature: 1970-1987, *J. Climate*, **8,** 1943–1957.

Seager, R., M.B. Blumenthal, and Y. Kushnir, 1995: An advective mixed layer model for ocean modeling purposes: global simulation of surface heat fluxes, *J. Climate*, **8,** 1951–1964.

Seager, R., S. Zebiak, and M.A. Cane, 1988: A model of the tropical Pacific sea surface temperature climatology, *J. Geophys. Res.*, **93,** 1265–1290.

Shriver, J.F., and H.E. Hurlburt, 1997: The contribution of the global thermohaline circulation to the Pacific to Indian Ocean throughflow via Indonesia, *J. Geophys. Res.*, **102,** 5491–5511.

Smedstad, O. M., and D. N. Fox, 1994: Assimilation of altimeter data in a 2-layer primitive equation model of the Gulf Stream, *J. Phys. Oceanogr.*, **24**, 305–325.

Smedstad, O. M., D. N. Fox, H. E. Hurlburt, G. A. Jacobs, E. J. Metzger, and J. L. Mitchell, 1997: Altimeter data assimilation into a $1/8°$ eddy resolving model of the Pacific Ocean, *J. Meteorol. Soc. Jpn.*, **75**, 429–444.

Stoica, P., and R. Moses, 1997: *Introduction to Spectral Analysis*, Prentice-Hall, Upper Saddle River, NJ.

Weller, R.A., M.F. Baumgartner, S.A. Josey, A.S. Fischer, and J.C. Kindle, 1998: Atmospheric forcing in the Arabian Sea during 1994-1995; observations and comparisons with climatology and models, *Deep Sea Res., Part B*, **45**, 1961–1999.

Weller, R.A., 1999: Woods Hole Oceanographic Institution, Woods Hole, Massachusetts, USA, *private communication*.

Young, D.K., and J.C. Kindle, 1994: Physical processes affecting availability of dissolved silicate for diatom production in the Arabian Sea, *J. Geophys. Res.*, **99**, 22,619–22,632.

Appendix A

OXYGEN-BASED DIAPYCNAL MIXING SCHEME

The global mixing correction scale factors Ω_k are set to rates of cross isopycnal mixing, based on oxygen saturation values S calculated at mean layer interface depths z_k. The rates of cross isopycnal mixing are determined in the same manner as Shriver and Hurlburt (1997), and the reader is referred to the latter for the physical rationale. In departure from this original approach, a different method is used here to blend the downward and upward vertical mixing rates that takes better account of the variation in oxygen saturation with depth. Here the depth (D_{min}) of the absolute minimum in oxygen saturation (S_{min}) is determined at each location, along with the greater depth (D_{base}) at which the oxygen saturation has increased to $S_{min} + 1$. These depths provide a better characterization of how the oxygen saturation varies with depth. They are used to linearly weight with depth the relative contributions of downward vertical mixing from the surface (w_d), and upward vertical mixing from the deep ocean (w_u).

The vertical mixing rates w_d and w_u are the same as in Shriver and Hurlburt (1997), and are repeated here to correct a couple of typographic errors.

$$w_d(t) = -\frac{\left(e^{-\alpha D_0} - e^{-\alpha z_k}\right)}{(1 - S/S_0)} \tag{A1}$$

$$w_u(t) = -\frac{\left(e^{-\alpha D_{2500}} - e^{-\alpha z_k}\right)}{(1 - S/S_{2500})} \tag{A2}$$

The notation is the same, except for the addition of D_0 and S_0 for the surface depth and oxygen saturation value, respectively. Here $D_0 = 0\,\mathrm{m}$, $D_{2500} = 2500\,\mathrm{m}$, and $\alpha = 3.5 \times 10^{-3}\,\mathrm{m}^{-1}$ also. The rates of vertical mixing are weighted across the region of the absolute minimum in the oxygen saturation profile such that

$$\Omega_k = \begin{cases} w_d & z_k < D_{min} \\ [(1 - \gamma_k)w_d + \gamma_k w_u] & D_{min} \leq z_k \leq D_{base} \ , \\ w_u & z_k > D_{base} \end{cases} \tag{A3}$$

where the weighting factor is $\gamma_k = (z_k - D_{min})/(D_{base} - D_{min})$. With this weighting choice, irregular regions of high mixing rates are removed in the fields obtained with the original method, and the fields vary smoothly with latitude and longitude in a manner consistent with the oxygen saturation climatology used (Levitus and Boyer 1994). This results in better global detrainment being applied in the NLOM simulations.

A1. REFERENCES

Levitus, S. and T. P. Boyer, 1994: World Ocean Atlas 1994. Volume 2: Oxygen. *NOAA Atlas NESDIS 2*, U.S. Department of Commerce, Washington, D.C.

Shriver, J. F., and H. E. Hurlburt, 1997: The contribution of the global thermohaline circulation to the Pacific to Indian Ocean throughflow via Indonesia, *J. Geophys. Res.*, **102**, 5491–5511.

Appendix B

NLOM NOTATION

The definitions of the symbols appearing in the many equations of this report are collected together below for ease of reference.

B1. Layer Model

The quantities appearing in the equations for the n active-layer reduced-gravity thermodynamic NLOM are defined below. The units used in the model are indicated in parentheses.

C_p	specific heat capacity for water, *cf* Table 2
$\mathbf{v}_k$	k$^{\text{th}}$ layer velocity (cm s^{-1})
ρ_k	k$^{\text{th}}$ layer density (σ_t)
h_k	k$^{\text{th}}$ layer thickness (m)
H_k	k$^{\text{th}}$ layer thickness at rest, *cf* Table 3
H_n	constant depth of ocean (6500 m)
ρ_n	constant rest density (27.71 σ_t)
f	Coriolis parameter (s^{-1})
ρ_0	constant reference density, *cf* Table 2
τ_w	wind stress
C_k	coefficient of interfacial friction
C_b	coefficient of bottom friction
ω_{kt}	entrainment mixing velocity due to turbulence (m/s)
$\tilde{\omega}_k$	k$^{\text{th}}$ interface reference (m s^{-1}) vertical mixing velocity
h_k^+	k$^{\text{th}}$ layer thickness at which entrainment starts (m)
h_k^-	k$^{\text{th}}$ layer thickness at which detrainment starts (m)
Ω_k	k$^{\text{th}}$ interface global mixing correction scale factor
C_M	coefficient additional interfacial friction associated with entrainment
A_H	coefficient of horizontal eddy viscosity (m^2 s^{-1})
K_H	coefficient of horizontal density diffusivity (m^2 s^{-1})
σ_ρ	reference coefficient of density climatology relaxation
$\widehat{\rho}_k$	k$^{\text{th}}$ layer density climatology
$\widehat{T}_k$	k$^{\text{th}}$ layer temperature climatology
H_o	constant reference density
$\Delta\rho_k^+$	minimum density contrast for $(\rho_{k+1} - \rho_k)$

$\alpha(T)$ coefficient of thermal expansion for sea water $(^\circ\mathrm{C}^{-1})$

$$\mathbf{V}_k = h_k \mathbf{v}_k$$

$$G_{kl} = \begin{cases} g(\rho_{n+1} - \rho_k)/\rho_0 & l \le k \\ g(\rho_{n+1} - \rho_l)/\rho_0 & l > k \end{cases}$$

$$\tau_k = \begin{cases} \tau_w & k = 0 \\ C_k \rho_0 |\mathbf{v}_k - \mathbf{v}_{k+1}| \times (\mathbf{v}_k - \mathbf{v}_{k+1}) & k = 1, 2, \ldots n \end{cases}$$

$$\omega_k = \begin{cases} 0 & k = 0, n \\ \left(\omega_k^+ + \delta_{1k} \omega_m^+ - \omega_k^- - \Omega_k \widehat{\omega}_k \right) & k = 1, 2, \ldots n \end{cases}$$

$$\omega_k^+ = \tilde{\omega}_k [\max(0, h_k^+ - h_k)/h_k^+]^2$$

$$\omega_k^- = \tilde{\omega}_k [\max(0, h_k - h_k^-)/h_k^+]^2$$

$$\omega_m^+ = \begin{cases} 0 & h_1 > h_m \\ \max(0, \omega_{kt}) & h_1 \le h_m \end{cases}$$

$$\widehat{\omega}_k = \int \int (\omega_k^+ - \omega_k^-) dS / \int \int \Omega_k dS; \ \ S(x,y) = \text{horizontal area of model domain}$$

$$\Delta \rho_k = \max(\rho_{k+1} - \rho_k - \Delta \rho_k^+, 0)$$

B2. Mixed Layer Model

The mixed layer equations of the model use the following notation:

T_m	temperature of mixed layer $(^\circ\mathrm{C})$
T_b	temperature beneath the base of the mixed layer $(^\circ\mathrm{C})$
h_m	mixed layer depth (m)
T_k	k^{th} layer temperature $(^\circ\mathrm{C})$
$\widehat{T}_k(x,y)$	k^{th} layer temperature clim. $(^\circ\mathrm{C})$
ω_m	vertical velocity at base of mixed layer $(\mathrm{m\,s}^{-1})$

B3. Turbulence Model

Enclosed below is the notation for the turbulence model equations:

m_i, n	turbulence model parameters, *cf* Table 2
f^+	Coriolis parameter at 5° latitude (s^{-1})
h_m^+	minimum mixed layer depth (m)
h_m^*	target mixed layer depth, $h_m^* \ge h_m^+$
ΔT	temperature contrast at base of mixed layer $(^\circ\mathrm{C})$

B4. Surface Heat Fluxes

The notation for the terms appearing in the surface heat flux equations are given here.

C_S	empirical coefficient for sensible heat flux
C_{pa}	specific heat capacity for air, *cf* Table 6
C_{L0}	intercept value for C_L coefficient
b	slope value for C_L coefficient ($^\circ\mathrm{C}^{-1}$)
ϵ	ratio of molecular weights of water vapor to dry air M_w/M_d
e_s	saturated water-vapor pressure (mb)
L	latent heat of evaporation of water, *cf* Table 6
P_a	air pressure, *cf* Table 6
$\Theta(x)$	Heaviside step function
$\widehat{T_a}$	climatological air temperature ($^\circ\mathrm{C}$)
$\widehat{q_a}$	climatological specific humidity of air
ρ_a	density of air, *cf* Table 6
$\widehat{v_a}$	scalar wind speed (m/s)
v_{min}	minimum scalar wind speed, *cf* Table 6

Appendix C

HEAT EQUATION

Heat energy within the NLOM is determined using a layer averaged form of the thermal energy equation. This equation is derived here because it differs in several respects from those used by other authors (McCreary et al. 1993).

Under the Boussinesq approximation, as used in the NLOM, the thermal energy equation for a fluid is given by (Kundu 1990)

$$\rho C_p \frac{DT}{Dt} = -\nabla \cdot \mathbf{q}, \tag{C1}$$

where T is temperature, ρ is the density, C_p is the specific heat capacity of sea water, q is the heat flux, and $D/Dt = \partial/\partial t + \mathbf{v} \cdot \nabla$ is the material time derivative. Viscous dissipation of energy is negligible in this approximation. We consider the heat flux to be the sum of a source at the air-sea interface, and an ocean component that obeys the Fourier law,

$$\nabla \cdot \mathbf{q} = \underbrace{-Q\delta(z)}_{\text{Term 1}} \underbrace{- \nabla \cdot \mathcal{K} \cdot \nabla T}_{\text{Term 2} \quad \text{Term 3}}, \tag{C2}$$

where Term 1 is the total heat flux, Term 2 the surface heat flux, and Term 3 the heat dissipation. The thermal conductivity $\mathcal{K}$ is a second-order tensor whose elements depend on the local state of the fluid. This heat dissipation term is similar in form to the viscous diffusion of momentum considered by Wajsowicz (1993). Following his same arguments, the tensor simplifies under the condition of transverse isotropy to a form having separate horizontal and vertical dependences (*cf* eq(11) in Wajsowicz (1993)). This yields after some rearrangement

$$\rho C_p \frac{\partial T}{\partial t} =$$
$$-\rho C_p \left(\mathbf{v} \cdot \nabla_H T - \omega \frac{\partial T}{\partial z} \right) + Q\delta(z)$$
$$+ \nabla_H \cdot (\mathcal{K}_H \nabla_H T) + \frac{\partial}{\partial z} \left(\mathcal{K}_V \frac{\partial T}{\partial z} \right), \tag{C3}$$

where ∇_H is the horizontal derivative, and z is the vertical coordinate. The latter is defined to increase positively with depth and is the reason the vertical advection term has opposite sign. Typical values used in ocean models for the vertical and horizontal thermal diffusivities are $\mathcal{K}_H = 300 \, \mathrm{m}^2 \, \mathrm{s}^{-1}$ (Hurlburt et al. 1996) and $\mathcal{K}_V = 2 \times 10^{-6} \, \mathrm{m}^2 \, \mathrm{s}^{-1}$ (Martin 1985), respectively. Corresponding typical horizontal and vertical length scales are $L = 10 \, \mathrm{km}$ and $d = 10 \, \mathrm{m}$. This implies that the vertical diffusion is negligible relative to the horizontal as $\mathcal{K}_V L^2 / \mathcal{K}_H d^2 \sim 7 \times 10^{-3}$. Only the contribution from horizontal diffusion is therefore retained.

The NLOM equations for ocean basin scales are derived by reducing the three-dimensional primitive equations to those for a two-dimensional model of a thin fluid on a spherical surface. They are formally obtained by integrating in the radial direction over the thickness of the spherical shell while considering the fluid state variables to be constant. Here we limit ourselves for simplicity to a Cartesian coordinate system to derive the general form of the equations, as the details on the integration procedure for the spherical case can be found elsewhere (Moore and Wallcraft 1997).

The heat equation for layer k is obtained by vertically integrating the thermal energy equation over the thickness $h_k = z_k^+ - z_k^-$ of the layer. Care must be taken when exchanging the order of derivatives and integrals because of the coordinate dependence on the integral limits. The relation for differentiation of a definite integral proves useful for this purpose (Gradshteyn and Ryzhik 1980).

$$
\frac{d}{d\alpha} \int_{\phi(\alpha)}^{\psi(\alpha)} f(x,\alpha)dx =
$$
$$
\left(\frac{d\psi}{d\alpha}\right) f(\psi(\alpha),\alpha) - \left(\frac{d\phi}{d\alpha}\right) f(\phi(\alpha),\alpha)
$$
$$
+ \int_{\phi(\alpha)}^{\psi(\alpha)} \frac{df(x,\alpha)}{d\alpha} dx \tag{C4}
$$

Straightforward application of this relation yields the layer averaged expressions for all but the diffusion term. The latter is a special case which we postpone until further below. We denote the diffusion for the time being by D_H. When integrating the vertical advection term a physical condition is applied when evaluating ωT at the layer interfaces z_k^+ and z_k^-. There must be no increase in the internal energy of the layer unless water of a different temperature is added to the layer. This leads to the layer heat equation

$$
\rho_k \frac{\partial(h_k T_k)}{\partial t} + \rho_k h_k \mathbf{v}_k \cdot \nabla_H T_k =
$$
$$
\delta_{1k} \frac{Q}{C_p} + \frac{D_H}{C_p} + \rho_k \left[\max(0,\omega_k)(T_{k+1} - T_k)\right.
$$
$$
\left. + \max(0,-\omega_{k-1})(T_{k-1} - T_k)\right] \tag{C5}
$$

in which $\omega_k = \partial z_k^+/\partial t$ is defined as the velocity of the interface between layers k and $k+1$.

The treatment of dispersion terms for layer models (D_H) is difficult because a physically consistent form cannot be directly derived from the primitive equation (Shchepetkin and O'Brien 1996). The alternative is to use a phenomenological form that best satisfies the constraints used in the general formulation of the three-dimensional stratified flow. The form $D_H = K_H \nabla_H \cdot (h_k \nabla_H T_k)$ follows naturally from the heat dissipation term in the primitive equation, with the spatial dependence of the thermal conductivity for the layer being made the same as the layer thickness $\mathcal{K}_k = K_H h_k$. It satisfies three of the constraints used in the general theory: 1) in the conservation form of the heat equation, the dispersion term must have the form of a divergence of a tensor; 2) the dispersion must be dissipative, implying the dissipation on the righthand side of the thermal energy equation has the form of divergence of a vector and a negatively defined source term; and 3) it depends on the symmetric part of a local tensor. In the case of momentum, the equivalent form of dispersion as lateral friction has been shown to give a tolerable solution (Shchepetkin and O'Brien 1996). The similarity of the primitive equations leads one to expect equivalent results for the thermal energy.

Using this choice for the dispersion term D_H, and the definition of thermal diffusivity $\kappa = K_H/(\rho C_p)$, one obtains the NLOM heat equation as follows:

$$\rho_k \frac{\partial(h_k T_k)}{\partial t} + \rho_k h_k \mathbf{v}_k \cdot \nabla_H T_k =$$
$$\delta_{1k} \frac{Q}{C_p} + \kappa \rho_k (\nabla_H \cdot (h_k \nabla_H)) T_k$$
$$+ \rho_k \left[\max(0, \omega_k)(T_{k+1} - T_k) \right.$$
$$+ \left. \max(0, -\omega_{k-1})(T_{k-1} - T_k) \right]. \qquad (C6)$$

The corresponding equation for the mixed layer is evident by inspection.

$$\rho_m \frac{\partial(h_m T_m)}{\partial t} + \rho_m h_m \mathbf{v}_1 \cdot \nabla_H T_m =$$
$$\frac{Q}{C_p} + \rho_m \max(0, \omega_m)(T_f - T_m)$$
$$+ \kappa \rho_m (\nabla_H \cdot (h_m \nabla_H)) T_m. \qquad (C7)$$

The mixed layer density ρ_m is determined from the mixed layer temperature via the relation

$$\rho_m = \widehat{\rho_1} - \alpha(\widehat{T_k}) \rho_o (T_m - \widehat{T_1}). \qquad (C8)$$

These equations are noted to differ from those of the MKM principally in the form of the advection and diffusion terms.

C1. REFERENCES

Gradshteyn, I.S., and I.M. Ryzhik (eds.), 1980: *Table of Integrals, Series, and Products*, 4th ed., Academic Press Inc., San Diego, CA.

Hurlburt, H.E., A.J. Wallcraft, W.J. Schmitz Jr., P.J. Hogan, and E.J. Metzger, 1996: Dynamics of the Kurosio/Oyashio current system using eddy-resolving models of the North Pacific Ocean, *J. Geophys. Res.,* **101,** 941–976.

Kundu, P.K., 1990: *Fluid Mechanics*, Academic Press Inc., San Diego, CA.

Martin, P.J., 1985: Simulation of the Mixed Layer at OWS November and Papa with several models, *J. Geophys. Res.,* **90,** 903–916.

McCreary, J.P., P.K. Kundu, and R.L. Molinari, 1993: A numerical investigation of dynamics, thermodynamics, and mixed-layer processes in the Indian Ocean, *Prog. Oceanogr.,* **31,** 181–244.

Moore, D.R. and A. J. Wallcraft, 1997: Formulation of the NRL Layered Ocean Model in Spherical Coordinates, *NRL Report CR 7323–96–0006*, Naval Research Laboratory, Stennis Space Center, Mississippi.

Shchepetkin, A.F. and J.J. O'Brien, 1996: A physically consistent formulation of lateral friction in shallow-water equation ocean models, *Mon. Wea. Rev.,* **124,** 1285–1300.

Wajsowicz, R.C., 1993: A consistent formulation of the anisotropic stress tensor for use in models of the large-scale ocean circulation, *J. Comp. Phys.*, **105,** 333–338.

Appendix D

GLOSSARY

The acronyms appearing throughout this report are listed below for ease of reference.

ATKE	Available turbulent kinetic energy
COADS	Comprehensive Ocean-Atmosphere Data Set
ECMWF	European Centre for Medium-Range Weather Forecast
FNMOC	Fleet Numerical Meteorology and Oceanography Center
HR	Hellerman and Rosenstein
IPOPS	Interim Primary Oceanographic Prediction System
MKM	McCreary and Kundu model
MLD	Mixed layer depth
NE	Northeast
NLOM	Naval Research Laboratory Layered Ocean Model
NOGAPS	Navy Operational Global Atmospheric Prediction System
NRL	Naval Research Laboratory
OGCM	Ocean general circulation model
PSD	Power spectral density
SS	Skill score
SSH	Sea surface height
SST	Sea surface temperature
SW	Southwest
TKE	Turbulent kinetic energy
VAWR	Vector-Averaging Wind Recorder
WHOI	Woods Hole Oceanographic Institution